



HAL
open science

Lagrangian dispersion and averaging behind a two-dimensional gaseous detonation front

Hiroaki Watanabe, Akiko Matsuo, Ashwin Chinnayya, Noboru Itouyama,
Akira Kawasaki, Ken Matsuoka, Jiro Kasahara

► **To cite this version:**

Hiroaki Watanabe, Akiko Matsuo, Ashwin Chinnayya, Noboru Itouyama, Akira Kawasaki, et al.. Lagrangian dispersion and averaging behind a two-dimensional gaseous detonation front. *Journal of Fluid Mechanics*, 2023, 968, pp.A28. 10.1017/jfm.2023.535 . hal-04261269

HAL Id: hal-04261269

<https://hal.science/hal-04261269>

Submitted on 26 Oct 2023

HAL is a multi-disciplinary open access archive for the deposit and dissemination of scientific research documents, whether they are published or not. The documents may come from teaching and research institutions in France or abroad, or from public or private research centers.

L'archive ouverte pluridisciplinaire **HAL**, est destinée au dépôt et à la diffusion de documents scientifiques de niveau recherche, publiés ou non, émanant des établissements d'enseignement et de recherche français ou étrangers, des laboratoires publics ou privés.

Banner appropriate to article type will appear here in typeset article

1 Lagrangian dispersion and averaging behind 2 two-dimensional gaseous detonation front

3 **Hiroaki Watanabe^{1,2}†, Akiko Matsuo³, Ashwin Chinnayya², Noboru Itouyama¹,**
4 **Akira Kawasaki¹, Ken Matsuoka¹, and Jiro Kasahara¹**

5 ¹Nagoya University, Furo-cho, Chikusa, Nagoya, Aichi, 464-8603, Japan

6 ²Institut Prime UPR 3346 CNRS, ENSMA, Universite de Poitiers, 1 avenue Clement Ader, BP 40109,
7 86961 Futuroscope-Chasseneuil CEDEX, France

8 ³Keio University, 3-14-1, Hiyoshi, Kohoku-ku, Yokohama, Kanagawa, 223-8522, Japan

9 (Received xx; revised xx; accepted xx)

10 Two-dimensional numerical simulations with the particle tracking method were conducted
11 to analyze the dispersion behind the detonation front and its mean structure. The mixtures
12 were $2\text{H}_2\text{-O}_2\text{-7 Ar}$ and $2\text{H}_2\text{-O}_2$ of increased irregularity in ambient conditions. The
13 detonation could be described as a two-scale phenomenon, specially for the unstable case.
14 The first scale is related to the main heat release zone, and the second where some classical
15 laws of turbulence remain relevant. The dispersion of the particles was promoted by the
16 fluctuations of the leading shock and its curvature, the presence of the reaction front, and
17 to a lesser extent transverse waves, jets, and vortex motion. Indeed, the dispersion and the
18 relative dispersion could be scaled using the reduced activation energy and the χ parameter,
19 respectively, suggesting that the main mechanism driving the dispersion came from the one-
20 dimensional leading shock fluctuations and heat release. The dispersion within the induction
21 time scale was closely related to the cellular structure, particles accumulating along the
22 trajectory of the triple points. Then, after a transient where the fading transverse waves and the
23 vortical motions coming from jets and slip lines were present, the relative dispersion relaxed
24 towards a Richardson-Obukhov regime, specially for the unstable case. Two new Lagrangian
25 Favre average procedures for the gaseous detonation in the instantaneous shock frame were
26 proposed and the mean profiles were compared with those from Eulerian procedure. The
27 characteristic lengths for the detonation were similar, meaning that the Eulerian procedure
28 gave the mean structure with a reasonable accuracy.

29 **Key words:** Detonations, Detonation waves

30 1. Introduction

31 Detonation is a supersonic premixed combustion wave, which consists of a leading shock
32 wave coupled with a reaction zone (Fickett and Davis 2000; Lee 2008; Zhang 2012),

† Email address for correspondence: watanabe0204@keio.jp

33 velocity of which is around several $\sim\text{mm}/\mu\text{s}$. Research on detonation is very active in
34 terms of propulsion application (Wolanski 2013; Anand and Gutmark 2019) and safety
35 engineering (Oran et al. 2020). Indeed, pressure increase downstream of the detonation
36 waves is very high. As such, the use of this combustion mode in a chamber may give
37 many advantages over conventional combustor based on deflagration. The Fickett-Jacob
38 cycle shows that higher thermal efficiency can be theoretically achieved. The compressor
39 and the combustion chamber may thus be more compact. On the other hand, unintentional
40 detonations imply severe damages to humans and goods.

41 Chapman-Jouguet (CJ) theory can predict the experimental detonation velocity in the ideal
42 case with great accuracy. A control volume embeds the leading shock and the state far from
43 the front where a chemical equilibrium is achieved. CJ velocity can be determined from the
44 fact that the propagation velocity is minimum. The fact that the CJ velocity can be calculated
45 from the initial conditions and the thermodynamic properties is the so-called Khariton's
46 principle, meaning that any material capable of exothermic reaction can detonate without
47 losses from boundaries (Higgins 2012).

48 Later, Zel'dovich, von Neumann and Döring (ZND) proposed the steady one-dimensional
49 model for the detonation structure. The induction reaction is triggered by the adiabatic
50 compression of the leading shock front, after which the exothermic reaction takes place. The
51 reactants are transformed into products, the deflagration zone traveling at the same velocity
52 than that of the shock. Characteristic lengths such as the induction and reaction lengths can
53 thus be estimated by the integration of the ZND model.

54 In contrast to the ZND model assumptions, detonation has an unsteady, multi-dimensional
55 cellular structure (Gamezo et al. 1999a; Austin 2003; Pintgen et al. 2003; Austin et al.
56 2005; Radulescu et al. 2005, 2007; Shepherd 2009; Kiyanda and Higgins 2013). The
57 cornerstone of the latter consists of an incident shock, a Mach stem and a transverse wave,
58 linked by a triple point, trajectory of which draws a fish cell like structure. The stronger Mach
59 stem and the weaker incident shock wave alternate in the propagation direction of the wave
60 front. The leading shock front velocity fluctuated around and 0.9-1.25 and 0.7-1.7 times the
61 CJ velocity in weakly unstable and unstable mixtures, respectively (Gamezo et al. 1999a).
62 Near the end of the cell, collision of transverse waves, propagating perpendicularly to the
63 leading shocks, may result in very high explosion centers. At a result of all these events, a
64 wide range of distribution of induction, reaction lengths and composition was present, due
65 to the exponential dependence of the chemical reaction rates on temperature (Austin 2003;
66 Pintgen et al. 2003; Austin et al. 2005).

67 From unsteady one-dimensional (1D) simulations, Ng et al. (2005a), Henrick et al.
68 (2006) and Romick et al. (2012) showed that the shock pressure followed a period-doubling
69 Feigenbaum scenario, through the increase of the reduced activation, with Abderrahmane et
70 al. (2011) determining that the corresponding chaos was deterministic. Shepherd (2009)
71 argued that the detonation could be statistically tractable. The hydrodynamic thickness x_{HT}
72 is the distance between the leading shock and the mean location of the sonic locus, although
73 the latter oscillated and did not strictly coincide any more with the end of the chemical
74 reaction (Kasimov and Stewart 2004; Stewart and Kasimov 2005). As such, this length can be
75 meant as a measure of the detonation driving zone (Short and Quirk 2018; Chiquete and Short
76 2019) that embeds in the multidimensional case the leading shock and the sonic surfaces.
77 Moreover, this length could be related to the dynamic parameters of detonation (Murray and
78 Lee 1983, 1985, 1986; Reynaud et al. 2020).

79 The hydrodynamic thickness was estimated from both experimental and numerical studies.
80 In experimental studies, the bow shock technique (Vasil'ev et al. 1972; Weber and Olivier
81 2003) or the decay of the pressure signal (Edwards et al. 1976; Jarsalé et al. 2016) were
82 used. Its estimation in numerical studies were determined by averaging the flow field (Lee and

83 Radulescu 2005; Radulescu et al. 2007) or by shortening the computational domain until the
84 effect of the rarefactions of the Taylor wave were no more effective (Gamezo et al. 1999b; Mi
85 et al. 2018). Gamezo et al. (1999a) investigated the effects of the reduced activation energy
86 on detonation, by comparing the Reynolds averages from simulations with the ZND results.
87 Later, Lee and Radulescu (2005) and Radulescu et al. (2007) proposed a Favre averaging
88 procedure in the mean shock frame. They revealed two important characteristic lengths,
89 associated with chemical exothermicity and the slower dissipation of the hydrodynamic
90 fluctuations, which govern the location of the average sonic surface, thus demonstrating the
91 usefulness of the statistical analysis for detonation. Furthermore, Sow et al. (2014) proposed
92 the Favre average procedure for the detonation in the non-inertial instantaneous shock frame
93 to take into account the unsteadiness of the shock front. So far, the Favre average procedure
94 to obtain one-dimensional profiles was applied to planar detonations (Lee and Radulescu
95 2005; Radulescu et al. 2007; Maxwell et al. 2017; Taileb et al. 2018, 2021; Sow et al. 2021),
96 in nonuniform mixtures (Mi et al. 2017a,b), in mixtures with concentration gradients (Han
97 et al. 2019), in mixtures with fluctuations in concentrations (Zhou et al. 2022), cylindrical
98 detonation (Han et al. 2017), also in non-ideal configurations such as detonations bounded
99 by an inert layer (Reynaud et al. 2017, 2020), with wall losses (Chinnayya et al. 2013; Sow
100 et al. 2014, 2015, 2019), and in two-phase detonations with water spray (Watanabe et al.
101 2019, 2020, 2021) and with fuel spray (Jourdain et al. 2022).

102 All these studies have extracted their one-dimensional profiles from straight lines parallel
103 to the direction of detonation propagation. However, Sow et al. (2021) showed that these
104 straight lines did not coincide with the material trajectories, due to convective mixing, which
105 increased with lower isentropic indexes, due to jet enhancement. Moreover, Borzou (2016)
106 and Radulescu (2018) tracked Lagrangian tracers, trajectories of which were affected by
107 the cellular structure of a single-headed detonation. These studies are the very few previous
108 investigations on dispersion behind detonation front, to the best of our knowledge. In addition,
109 the comparison between Lagrangian and Eulerian averaging processes has not been done
110 yet.

111 In order to address this issue, unsteady two-dimensional simulations with the Lagrangian
112 particle tracking method were conducted for detonation in a straight channel for two mixtures
113 of increased irregularity. Both the distance traveled by the Lagrangian particle behind the
114 front and the time from shock passage were recorded in the course of the simulations. The
115 degree of the dispersion and the relative dispersion (Babiano et al. 1990; Sawford 2001;
116 Salazar and Collins 2009) were evaluated. Two new Favre average procedures, based on
117 the distance traveled by the Lagrangian particle or the time from the shock passage were
118 proposed to assess the accuracy of the previous Eulerian Favre average procedure.

119 The plan of this paper is as follows. The governing equations and the numerical method
120 are presented in Section 2.1 and 2.2, respectively. The procedure to record the values for each
121 Lagrangian particle is explained in Section 2.3. Section 3 describes the problem statement.
122 The results and discussions are given in Section 4. The dispersion behind the detonation
123 front and the anisotropic motion are firstly examined in Section 4.1. Then, the dispersion
124 in the induction time scale is analyzed in Section 4.2. Furthermore, the relative dispersion
125 is discussed in Section 4.3. Moreover, the two new Lagrangian Favre average procedures
126 are described and the 1D profiles from these procedures are compared with the Eulerian
127 estimates in Section 4.4. Finally, the main conclusions are drawn in Section 5.

128 2. Numerical setup

129

2.1. Governing equations

130 The governing equations for the gaseous phase are the two-dimensional (2D) reactive
 131 compressible Navier-Stokes equations, with the ideal equation of state. The chemical reaction
 132 mechanism proposed by Hong et al. (2011), which considers 9 species (H_2 , O_2 , H , O , OH ,
 133 H_2O , HO_2 , H_2O_2 and Ar) and 20 elemental reactions, is used. In addition, the reliable
 134 performance of this detailed chemical reaction mechanism can be achieved over a range
 135 of the reactant concentrations, stoichiometries, pressures, and temperature from 950 K to
 136 greater than 3000 K according to the validation by Hong et al. (2011).

$$137 \quad \frac{\partial \mathbf{U}}{\partial t} + \frac{\partial \mathbf{E}}{\partial x} + \frac{\partial \mathbf{F}}{\partial y} + \frac{\partial \mathbf{E}_d}{\partial x} + \frac{\partial \mathbf{F}_d}{\partial y} = \mathbf{S} \quad (2.1)$$

$$138 \quad \mathbf{U} = \begin{bmatrix} \rho \\ \rho u \\ \rho v \\ e \\ \rho Y_k \end{bmatrix}, \mathbf{E} = \begin{bmatrix} \rho u \\ \rho u^2 + p \\ \rho uv \\ (e + p)u \\ \rho Y_k u \end{bmatrix}, \mathbf{F} = \begin{bmatrix} \rho v \\ \rho uv \\ \rho v^2 + p \\ (e + p)v \\ \rho Y_k v \end{bmatrix}$$

$$139 \quad \mathbf{E}_d = \begin{bmatrix} 0 \\ -\tau_{xx} \\ -\tau_{xy} \\ -\tau_{xx}u - \tau_{xy}v + q_x \\ j_{x,k} \end{bmatrix}, \mathbf{F}_d = \begin{bmatrix} 0 \\ -\tau_{yx} \\ -\tau_{yy} \\ -\tau_{yx}u - \tau_{yy}v + q_y \\ j_{y,k} \end{bmatrix}, \mathbf{S} = \begin{bmatrix} 0 \\ 0 \\ 0 \\ 0 \\ \dot{\omega}_k \end{bmatrix}$$

$$140 \quad p = \rho RT \quad (2.2)$$

141 Here, x , y , t , ρ , u , v , p , T , e , Y_k and $R = R_u (\sum_{k=1}^{N_s} Y_k / W_k)$ are longitudinal coordinate,
 142 transverse coordinate, time, density, velocity in x direction, velocity in y direction, pressure,
 143 temperature, total energy, mass fraction of species k and gas constant, respectively. N_s , R_u ,
 144 and W_k are the total number chemical species, universal gas constant, and molecular weight
 145 of species k . τ , q , j_k and $\dot{\omega}_k$ denote the shear stress, heat flux, diffusion flux, and reaction
 146 rate, respectively. The total energy can be written as the following formula.

$$147 \quad e = \sum_{k=1}^{N_s} \rho Y_k h_k - p + \frac{1}{2} \rho (u^2 + v^2) \quad (2.3)$$

148 Here, h_k is enthalpy for species k . The Stokes' hypothesis is utilized and the bulk viscosity
 149 can be neglected. The shear stress is expressed as

$$150 \quad \tau_{xx} = \frac{2}{3} \mu \left(2 \frac{\partial u}{\partial x} - \frac{\partial v}{\partial y} \right) \quad (2.4)$$

$$151 \quad \tau_{xy} = \tau_{yx} = \mu \left(\frac{\partial u}{\partial y} + \frac{\partial v}{\partial x} \right) \quad (2.5)$$

$$152 \quad \tau_{yy} = \frac{2}{3} \mu \left(2 \frac{\partial v}{\partial y} - \frac{\partial u}{\partial x} \right) \quad (2.6)$$

153 Here, μ is viscosity. The heat flux is the sum of the heat flux by the temperature gradient
 154 (i.e., Fourier's law) and the heat flux by the enthalpy transport. The heat flux caused by

155 concentration gradients, i.e. Dufour effect, is neglected in this study because Dufour effect
156 is negligibly small in the combustion process (Warntz et al. 2006).

$$157 \quad q_x = -\kappa \frac{\partial T}{\partial x} - \rho \sum_{k=1}^{N_s} h_k D_k \frac{\partial Y_k}{\partial x} \quad (2.7)$$

158

$$159 \quad q_y = -\kappa \frac{\partial T}{\partial y} - \rho \sum_{k=1}^{N_s} h_k D_k \frac{\partial Y_k}{\partial y} \quad (2.8)$$

160 Here, κ and D_k are thermal conductivity and diffusion coefficient for species k . The diffusive
161 flux is evaluated using Fick's law as the following equations

$$162 \quad j_{x,k} = -\rho D_k \frac{\partial Y_k}{\partial x} \quad (2.9)$$

$$163 \quad j_{y,k} = -\rho D_k \frac{\partial Y_k}{\partial y} \quad (2.10)$$

164 The diffusive flux caused by temperature gradient, i.e. Soret effect, is neglected in this
165 study. The Soret effect is only important for light species and at low temperature (Warntz
166 et al. 2006) so that its effect will be negligible for the propagation of detonation wave and
167 the flow field behind the front. D_k used in Eqs. 2.9 and 2.10 is evaluated by the mixing
168 rule for the diffusive flux in terms of the mass fraction (Kee et al. 2003) (see Eq. 2.31)
169 so that the expression for the diffusive flux in mixture average evaluation is consistent. The
170 correction velocity to ensure that the summation of the diffusive fluxes is zero was not
171 taken into account in our computations. Indeed, the magnitude of correction is significantly
172 small (Reaction Design 2000). Moreover, in order to ensure that the summation of the mass
173 fractions to be one numerically, each mass fraction was normalized by the summation of the
174 mass fractions, after the numerical integration.

175 The thermodynamic properties such as enthalpy h_k , specific heat at the constant pressure
176 $c_{p,k}$ and entropy s_k^0 for species k are assumed to be function of temperature and are determined
177 from the Janaf thermochemical polynomials (McBride et al. 1993).

$$178 \quad \frac{h_k}{(R_u/W_k)T} = a_{1,k} + \frac{a_{2,k}}{2}T + \frac{a_{3,k}}{3}T^2 + \frac{a_{4,k}}{4}T^3 + \frac{a_{5,k}}{5}T^4 + \frac{a_{6,k}}{T} \quad (2.11)$$

$$179 \quad \frac{c_{p,k}}{R_u/W_k} = a_{1,k} + a_{2,k}T + a_{3,k}T^2 + a_{4,k}T^3 + a_{5,k}T^4 \quad (2.12)$$

$$180 \quad \frac{s_k^0}{R_u/W_k} = a_{1,k} \ln T + a_{2,k}T + \frac{a_{3,k}}{2}T^2 + \frac{a_{4,k}}{3}T^3 + \frac{a_{5,k}}{4}T^4 + a_{7,k} \quad (2.13)$$

181 Here, $a_{1,k}$, $a_{2,k}$, $a_{3,k}$, $a_{4,k}$, $a_{5,k}$, $a_{6,k}$, and $a_{7,k}$ are the coefficient depending on the species
182 k and temperature range ($T < 1000$ K or $T \geq 1000$ K).

183 From a preliminary study, a method proposed by Gordon et al. (1984) is shown to be
184 accurate compared to the experimental data as for the viscosity and thermal conductivity.
185 However, the coefficients for HO_2 in a method proposed by Gordon et al. (1984) are not
186 available. As for the transport properties of viscosity μ_k and thermal conductivity κ_k for
187 species k apart from HO_2 , a method proposed by Gordon et al. (1984) is used to estimate
188 the gas viscosity and thermal conductivity as the following equations.

$$\ln \mu_k = C_{1,k}^\mu \ln T + \frac{C_{2,k}^\mu}{T} + \frac{C_{3,k}^\mu}{T^2} + C_{4,k}^\mu \quad (2.14)$$

$$\ln \kappa_k = C_{1,k}^\kappa \ln T + \frac{C_{2,k}^\kappa}{T} + \frac{C_{3,k}^\kappa}{T^2} + C_{4,k}^\kappa \quad (2.15)$$

Here, $C_{1,k}^\mu$, $C_{2,k}^\mu$, $C_{3,k}^\mu$, $C_{4,k}^\mu$, $C_{1,k}^\kappa$, $C_{2,k}^\kappa$, $C_{3,k}^\kappa$, and $C_{4,k}^\kappa$ are the coefficient depending on the species k and temperature range ($T < 1000$ K or $T \geq 1000$ K).

The viscosity and thermal conductivity for HO₂ are calculated from the Chapman-Enskog method (Chapman and Cowling 1991) and the Eucken method (Poling et al. 2001), respectively.

The viscosity for HO₂ is evaluated by the Chapman-Enskog method (Chapman and Cowling 1991) by the equation 2.16.

$$\mu_{\text{HO}_2} = 2.6693 \times 10^{-6} \frac{\sqrt{W_{\text{HO}_2} T}}{\sigma_{\text{HO}_2}^2 \Omega_{22}} \quad (2.16)$$

Here, σ_{HO_2} and Ω_{22} are the Lennard-Jones collision diameter for HO₂ and the collision integral, respectively. The collision integrals Ω_{22} are calculated from the following empirical formula suggested by Neufeld et al. (1972). (see Eq. 2.17)

$$\Omega_{22} = C_1^{22} (T^*)^{-C_2^{22}} + C_3^{22} \exp(-C_4^{22} T^*) + C_5^{22} \exp(-C_6^{22} T^*) \quad (2.17)$$

Here, the constants in Eq. 2.17 are defined as follows. $C_1^{22} = 1.16145$, $C_2^{22} = 0.14874$, $C_3^{22} = 0.52487$, $C_4^{22} = 0.77320$, $C_5^{22} = 2.16178$, $C_6^{22} = 2.43787$. T^* is the reduced temperature given by Eq. 2.18.

$$T^* = \frac{k_B T}{\varepsilon_k} \quad (2.18)$$

Here, ε_k and k_B are the Lennard-Jones potential well depth for species k and the Boltzmann constant, respectively. The thermal conductivity for HO₂ is evaluated by the Eucken method (Poling et al. 2001) as

$$\kappa_{\text{HO}_2} = \frac{7}{2} R_u \mu_{\text{HO}_2} \quad (2.19)$$

The Wilke method (Wilke 1958) and the Wassiljewa method (Law 2006) are used to estimate the multi-component gas viscosity and thermal conductivity based on the pure species values.

$$\mu = \sum_{k=1}^{N_s} \frac{\mu_k}{1 + \frac{1}{X_k} \sum_{l \neq k}^{N_s} X_l \Phi_{kl}} \quad (2.20)$$

$$\kappa = \sum_{k=1}^{N_s} \frac{\kappa_k}{1 + \frac{1.065}{X_k} \sum_{l \neq k}^{N_s} X_l \Phi_{kl}} \quad (2.21)$$

Here, X_k is the molar fraction for species k and Φ_{kl} is calculated as

$$\Phi_{kl} = \frac{[1 + (\mu_k/\mu_l)^{1/2}(W_l/W_k)^{1/4}]^2}{2\sqrt{2}(1 + W_k/W_l)^{1/2}} \quad (2.22)$$

The diffusion coefficient of a compound k into the mixture of the other compounds is evaluated based on the binary diffusion coefficient between the species k and l from the Chapman-Enskog method (Chapman and Cowling 1991). The binary diffusion coefficient between the species k and l is the function of temperature and pressure and expressed as the following formula.

$$D_{kl} = 2.628 \times 10^{-2} \frac{\sqrt{T^3}}{p\sigma_{kl}^2\Omega_{11}} \sqrt{\frac{(W_k + W_l)}{2W_kW_l}} \quad (2.23)$$

Here, σ_{kl} and Ω_{11} are the effective collision diameter for species k and l , and the collision integral. The collision integral Ω_{11} is estimated by the following empirical formula (Neufeld et al. 1972).

$$\Omega_{11} = \frac{C_1^{11}}{(T_d^*)^{C_2^{11}}} + \frac{C_3^{11}}{\exp(C_4^{11}T_d^*)} + \frac{C_5^{11}}{\exp(C_6^{11}T_d^*)} + \frac{C_7^{11}}{\exp(C_8^{11}T_d^*)} \quad (2.24)$$

$$T_d^* = \frac{k_B T}{\varepsilon_{kl}} \quad (2.25)$$

Here, the constants in Eq. 2.24 are defined as follows. $C_1^{11} = 1.06036$, $C_2^{11} = 0.15610$, $C_3^{11} = 0.19300$, $C_4^{11} = 0.47635$, $C_5^{11} = 1.03587$, $C_6^{11} = 1.52996$, $C_7^{11} = 1.76474$, $C_8^{11} = 3.89411$. ε_{kl} is the effective Lennard-Jones potential well depth for species k and l . σ_{kl} and ε_{kl} are estimated based on the Lennard-Jones collision diameter and Lennard-Jones potential well depth for species k and l , and the formula is different depending on whether the collision partners are polar or nonpolar. For the case that the partners are either both polar or both nonpolar, the equations are

$$\varepsilon_{kl} = \sqrt{\varepsilon_k \varepsilon_l} \quad (2.26)$$

$$\sigma_{kl} = \frac{\sigma_k \sigma_l}{2} \quad (2.27)$$

Here, ε_k , ε_l are the Lennard-Jones collision potential well depth for species k and l , respectively. σ_k and σ_l are the Lennard-Jones collision diameter for species k and l , respectively. For the case for a polar molecule interacting with a nonpolar molecule, the equations are

$$\varepsilon_{kl} = \xi^2 \sqrt{\varepsilon_k \varepsilon_l} \quad (2.28)$$

$$\sigma_{kl} = \frac{\sigma_k \sigma_l}{2} \xi^{-\frac{1}{6}} \quad (2.29)$$

$$\xi = 1 + \frac{1}{4} \alpha_{np}^* \mu_{pol}^* \sqrt{\frac{\varepsilon_{pol}}{\varepsilon_{np}}} \quad (2.30)$$

Here, α_{np}^* and μ_{pol}^* are the reduced polarizability for the nonpolar molecule and the reduced dipole moment for the polar molecule, respectively. The subscripts for np and pol in Eq. 2.30

247 denote the nonpolar and polar molecule, respectively. The diffusion coefficient of a compound
 248 k into the mixture of the other compound D_k to estimate the diffusive flux using the mass
 249 fraction gradient is calculated by the following mixing rule (Kee et al. 2003).

$$250 \quad D_k = \frac{1}{\sum_{l \neq k}^{N_s} \frac{X_l}{D_{kl}} + \frac{X_k}{1 - Y_k} \sum_{l \neq k}^{N_s} \frac{Y_l}{D_{kl}}} \quad (2.31)$$

251 The trajectories of the gas particles can be simply obtained by massless Lagrangian
 252 particles with the following equations Eqs.2.32 and 2.33.

$$253 \quad \frac{dx_{p,i}}{dt} = u_i \quad (2.32)$$

$$254 \quad \frac{dy_{p,i}}{dt} = v_i \quad (2.33)$$

256 Here, $x_{p,i}$ and $y_{p,i}$ are the x position and y positions for the i^{th} Lagrangian particle. u_i and v_i
 257 are the x and y components of the velocity at the i^{th} particle position, respectively.

258 *2.2. Numerical methods*

259 The detailed formulation of the numerical method can be found in Watanabe (2020). A
 260 classical first order operator-splitting method is employed to couple the hydrodynamics with
 261 the detail chemistry. The spatial derivatives of the convective term are discretized by fifth
 262 order advection upstream splitting method using pressure based weight functions (known
 263 as AUSMPW+) improved by Kim et al. (2001) based on a modified weighted essentially
 264 non-oscillatory scheme (known as MWENO-Z) (Hu et al. 2016) and a second-order central
 265 differential scheme is applied to the discretization of the diffusive term. The time integration
 266 method for the convective and diffusion terms is the third order total variation diminishing
 267 Runge-Kutta method (Gottlieb et al. 2001), and the multi-time-scale method (Gou et al.
 268 2010) is used for the time integration of the chemical source term.

269 The first order Euler method is used for the integration of the Lagrangian particles. The
 270 gas phase quantities around the i^{th} Lagrangian particle ψ_i are estimated by interpolating the
 271 surrounding three nearby Eulerian cell values by the barycentric interpolation (Shimura and
 272 Matsuo 2018) as follows (see Eq. 2.34).

$$273 \quad \psi_i = c_1 \psi_1 + c_2 \psi_2 + c_3 \psi_3 \quad (2.34)$$

274 Here, ψ_1 , ψ_2 and ψ_3 are the gas phase quantities at three Eulerian cells nearby the i^{th}
 275 Lagrangian particle, respectively. c_1 , c_2 and c_3 are the normalized coefficient which is
 276 estimated based on the ratio of area of the triangles to the area of the cell (Shimura and
 277 Matsuo 2018; Watanabe 2020).

278 *2.3. Recording the variables for each Lagrangian particle*

279 The variables of each Lagrangian particle were recorded during the course of their trajecto-
 280 ries, being updated every time step. The time when the Lagrangian particles passed the leading
 281 shock front t_{shock} was recorded by the first pressure jump experienced by the Lagrangian
 282 particles to estimate the time from the shock passage $\tau = t - t_{\text{shock}}$. The dispersion of the
 283 Lagrangian particles were evaluated by the distance traveled by the Lagrangian particle after
 284 the shock passage from Eqs. 2.35, 2.36 and 2.37. The equations 2.35 and 2.36 refer to the
 285 longitudinal and transverse distances traveled by the Lagrangian particle after the shock
 286 passage, respectively. Equation 2.37 represents the distance traveled by the Lagrangian
 287 particle after the shock passage.

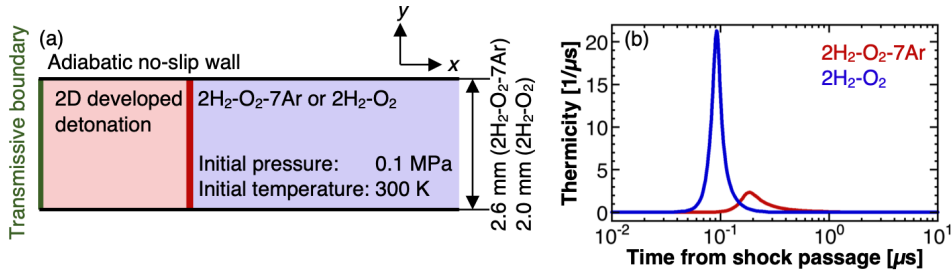


Figure 1: Simulation setup. (a) Schematics of the computational target, (b) ZND thermicity profile in 2H₂-O₂-7Ar and 2H₂-O₂ mixtures.

$$x_i = \int u_i dt \quad (2.35)$$

$$y_i = \int |v_i| dt \quad (2.36)$$

$$x_{xy,i} = \int (u_i^2 + v_i^2)^{1/2} dt \quad (2.37)$$

Tracking of the Lagrangian particles enabled to obtain the time when the induction process was completed. The thermicity $\dot{\sigma}$, which denotes the influence of chemical reaction on the flow velocity due to both chemical energy release and change in the number of moles present, was used to define the induction time. The thermicity was defined by following equation 2.38 and calculated based on the variables at each Lagrangian particle position.

$$\dot{\sigma} = \sum_{k=1}^{N_s} \left(\frac{W}{W_k} - \frac{h_k}{c_p T} \right) \frac{\dot{\omega}_k}{\rho} \quad (2.38)$$

During the simulation, the time, the x - and y -Lagrangian particle positions, and the distance traveled by Lagrangian particle when the thermicity was maximum were recorded and updated every time step. The induction time was defined as the time from the shock front to the time when the thermicity was maximum in this study. With the use of the Lagrangian particle tracking method, the induction time for each Lagrangian particle can be accurately evaluated from the difference between the time when the Lagrangian particle passed the leading shock front and the time when the thermicity was maximum.

3. Problem statement

The schematics for the computational target is shown in Fig. ??(a). The fully developed two-dimensional gaseous detonation propagates in a straight channel. Two types of reactive mixtures have been investigated: 70% diluted stoichiometric hydrogen oxygen mixture 2H₂-O₂-7Ar and stoichiometric hydrogen oxygen mixture 2H₂-O₂ at ambient conditions (0.1 MPa and 300 K). The effect of instabilities can thus be assessed on the dispersion and the averaging processes. Figure ??(b) shows the thermicity profile for both mixtures. Table 1 lists the various parameters for both mixtures characterizing detonation such as the CJ velocity D_{CJ} , the CJ Mach number M_{CJ} , the induction length x_{ind} , the reaction length x_{reac} , the induction time τ_{ind} , the reaction time τ_{reac} , the reduced activation energy $E_a/(RT_{vN})$, the $\chi = E_a/(RT_{vN}) \cdot x_{ind}/x_{reac}$ parameter, and the specific heat ratio at von Neumann (vN) state γ_{vN} . Following the definition by Radulescu (2003) and Ng et al. (2005b), the induction

Parameters	2H ₂ -O ₂ -7Ar	2H ₂ -O ₂
D_{CJ} [m/s]	1690.7	2834.3
M_{CJ}	4.8	5.3
x_{ind} [μ m]	76.6	48.6
x_{reac} [μ m]	409	72.5
τ_{ind} [μ s]	0.2	0.09
τ_{reac} [μ s]	0.1	0.02
$E_a/(RT_{vN})$	4.1	6.9
χ	0.8	4.6
γ_{vN}	1.49	1.32

Table 1: Parameters of the reactive mixtures in the present conditions.

length x_{ind} was defined as the distance from the leading shock front to the position where the thermicity was maximum, and the reaction length x_{reac} was estimated by $u_{CJ}/\dot{\sigma}_{max}$ using the maximum thermicity $\dot{\sigma}_{max}$ and the velocity at the CJ plane in the shock frame u_{CJ} . In addition, the induction time τ_{ind} was estimated from the time from the leading shock front to the time when thermicity was maximum, and the reaction time τ_{reac} was defined as the half pulse width time of thermicity, respectively. The induction time for 2H₂-O₂ mixture is about 2 times shorter than that for 2H₂-O₂-7Ar mixture and the peak thermicity for 2H₂-O₂ is about 1 order magnitude higher compared to that for 2H₂-O₂-7Ar mixture in the present conditions (Fig. ??(b) and Table 1). The mixtures can be classified as weakly and mildly unstable mixture, according to the stability analysis (Eckett et al. 2000; Austin et al. 2005) based on the reduced activation energy and CJ Mach number. Based on the χ parameter and CJ Mach number, the instability parameters lie slightly below and above the neutral stability curve, for the diluted and non diluted cases (Ng et al. 2005b).

The channel widths for 2H₂-O₂-7Ar and 2H₂-O₂ mixtures are 2.6 mm and 2.0 mm, respectively. The boundary condition for the walls is the adiabatic non-slip wall and the transmissive boundary is applied to the left end. The grid is uniform and the grid width is equal at 2.0 μ m and 1.6 μ m from the region from the shock front up to 20.6 mm and 11.5 mm behind the front for the 2H₂-O₂-7Ar mixture and 2H₂-O₂ mixture, respectively. The computational domain with the minimum grid width encompassed the mean leading shock front and the mean sonic plane, which were evaluated in the Section 4.4. Then, the grid is stretched. The grid resolution is about 38 and 30 points per CJ induction length for 2H₂-O₂-7Ar mixture and 2H₂-O₂ mixture, respectively. This resolution has been shown to be largely sufficient to capture the mean structure (Reynaud et al. 2017, 2020). In addition, this resolution is enough to reproduce the features of the instantaneous flow fields for weakly unstable mixture (Mazaheri et al. 2012). The grid resolution study was performed in Appendix A and the main conclusions were not called into question by the present grid resolution. For more highly unstable mixtures, this resolution may not be sufficient to capture the unsteady burning mechanism of the unburnt pockets that are likely to form downstream of the leading shocks. The Courant-Friedrichs-Lewy number was fixed at 0.2 and the typical time step size was around 1.0×10^{-10} s and 0.5×10^{-10} s for 2H₂-O₂-7Ar and 2H₂-O₂ mixtures, respectively.

The recycling block technique (Sow et al. 2019) is applied to enable the detonation to propagate a distance long enough to obtain statistical values. When the leading shock front reached the right boundary during the simulations, the new region with the upstream condition for unburned state was appended to the right of the computational domain and

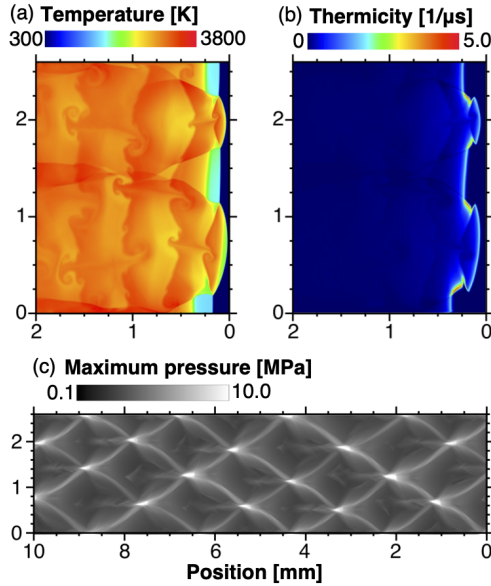


Figure 2: 2D instantaneous flow fields in $2\text{H}_2\text{-O}_2\text{-7Ar}$ mixture. (a) Temperature, (b) thermicity, (c) maximum pressure.

352 the region near the left boundary which was far from the mean sonic plane was discarded.
 353 The same procedure was also applied for the Lagrangian particles. When the leading shock
 354 front reached the right boundary during the simulations, the new Lagrangian particles were
 355 located to the right of the computational domain and the Lagrangian particles which were
 356 located in the discarded left domain were excluded from the simulations. The recycling
 357 block technique was successfully utilized to reduce the computational cost by the use of
 358 smaller computational domain and to simulate the detonation propagation in the previous
 359 studies (Reynaud et al. 2017, 2020; Sow et al. 2019; Taileb et al. 2020, 2021; Watanabe et
 360 al. 2020, 2021). The length of the propagation for the average procedure is about $1000 x_{\text{ind}}$
 361 for $2\text{H}_2\text{-O}_2\text{-7Ar}$ and $1200 x_{\text{ind}}$ for $2\text{H}_2\text{-O}_2$. This study has cost about 2.0 million CPU
 362 hours with 64 processors.

363 The Lagrangian particles are initially located in the fresh mixture in every grid point. The
 364 number of these particles inside the computational domain changes during the simulation due
 365 to the recycling block method and are around 34 millions and 25 millions for $2\text{H}_2\text{-O}_2\text{-7Ar}$
 366 mixture and $2\text{H}_2\text{-O}_2$ mixture, respectively. In order to get the averaged values, the
 367 instantaneous 2D flow fields are saved each time the detonation front propagates $0.5 x_{\text{ind}}$. The
 368 total number of the particles in the region where the detonation propagates is about 5×10^7
 369 and 6×10^7 for $2\text{H}_2\text{-O}_2\text{-7Ar}$ and $2\text{H}_2\text{-O}_2$ mixtures, respectively.

370 4. Results and discussions

371

4.1. Dispersion and anisotropy

372 Firstly, the global features of $2\text{H}_2\text{-O}_2\text{-7Ar}$ and $2\text{H}_2\text{-O}_2$ mixtures are depicted using the
 373 instantaneous 2D flow fields in Figs. 2 and 3, respectively. In $2\text{H}_2\text{-O}_2\text{-7Ar}$ mixture,
 374 the cellular structure is regular with two cells in the channel (Fig. 2(c)). No unburned gas pocket
 375 is formed behind the front and the classical key stone feature can be observed (Figs. 2(a,b)).
 376 As for $2\text{H}_2\text{-O}_2$ mixture, the cellular structure and the frontal shape were more irregular
 377 (Fig. 3), expected from the increased instability parameters. The unburned gas pockets are

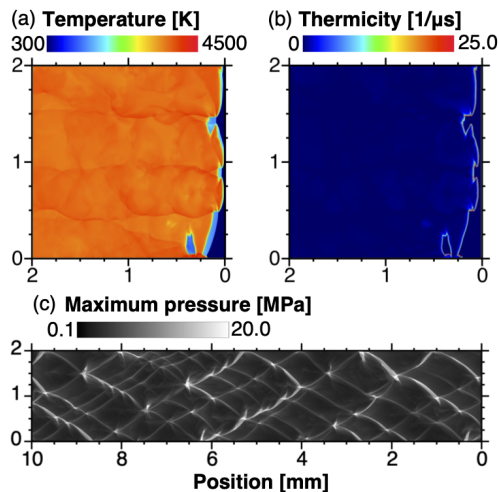


Figure 3: 2D instantaneous flow fields in $2\text{H}_2\text{-O}_2$ mixture. (a) Temperature, (b) thermicity, (c) maximum pressure.

378 torn apart from the front and continue to burn downstream (Figs. 3(a,b)). In both cases,
 379 strong transverse wave structures occurred in the second part of the cell (Figs. 2(b)3(b)),
 380 as also observed experimentally by Desbordes and Presles (2012). The thermicity fields
 381 indicated that the heat release took place much more rapidly and sometimes one order of
 382 magnitude quicker in the non-diluted case than in the diluted case (Figs. 2(b)3(b)). The
 383 average propagation velocity for both mixtures agreed with that of the CJ velocity. The
 384 average cell width in the simulations from the manual measurement of 150 and 300 cells for
 385 $2\text{H}_2\text{-O}_2\text{-7Ar}$ and $2\text{H}_2\text{-O}_2$ mixtures is 1.3 mm and 0.7 mm, respectively. The experimental cell
 386 width for $2\text{H}_2\text{-O}_2\text{-7Ar}$ mixture is expected to be 2.7-4.0 mm from similar mixture conditions,
 387 and the cell width reported from experiments for $2\text{H}_2\text{-O}_2$ mixture ranges from 1.4 mm to
 388 2.1 mm (Kaneshige and Shepherd 1997). Therefore, the cell sizes in the simulations were
 389 thus smaller than the experimental ones by a factor of about 2-3. The numerical cell width is
 390 reported to be smaller as in previous studies (Taylor et al. 2013; Taïleb et al. 2020). This
 391 is not due to the present numerical resolution but may be due to vibrational non-equilibrium
 392 effects (Taylor et al. 2013; Shi et al. 2017), uncertainties of the chemical reaction model in
 393 detonation conditions (Mével and Gallier 2018) and three-dimensional effects (Taïleb et al.
 394 2018; Monnier et al. 2022; Crane et al. 2023).

395 Figures 4 and 5 show the instantaneous 2D flow fields in the Lagrangian perspective for (a)
 396 time front shock passage; (b) longitudinal distance traveled by the particle x_i , (c) transverse
 397 distance traveled by the particle y_i , (d) distance traveled by the particle $x_{xy,i}$ from shock
 398 passage for $2\text{H}_2\text{-O}_2\text{-7Ar}$ and $2\text{H}_2\text{-O}_2$ mixtures, respectively. As we move away from
 399 the leading shocks, the time from shock passage and the longitudinal distance x_i increased.
 400 However, their distributions were not uniform in each section, regardless of the mixture
 401 instability. This non uniform distribution of the Lagrangian particles is consistent with the
 402 numerical findings of Sow et al. (2021). The scales of the legends for Figs. 4(a) and 5(a)
 403 are different, due to the difference in detonation velocities for both mixtures. It can also be
 404 seen that x_i and $x_{xy,i}$ were almost the same, due to the fact that y_i remained one order of
 405 magnitude lower. In the rest of the paper, only the field of x_i will be discussed instead of
 406 that of $x_{xy,i}$. More noticeable was that the transverse distance y_i was much more spotty for
 407 the non-diluted case, as we moved away from the leading shocks, indicative of more vortical
 408 structures. Large tongues of gas were also seen to penetrate the different layers and to be

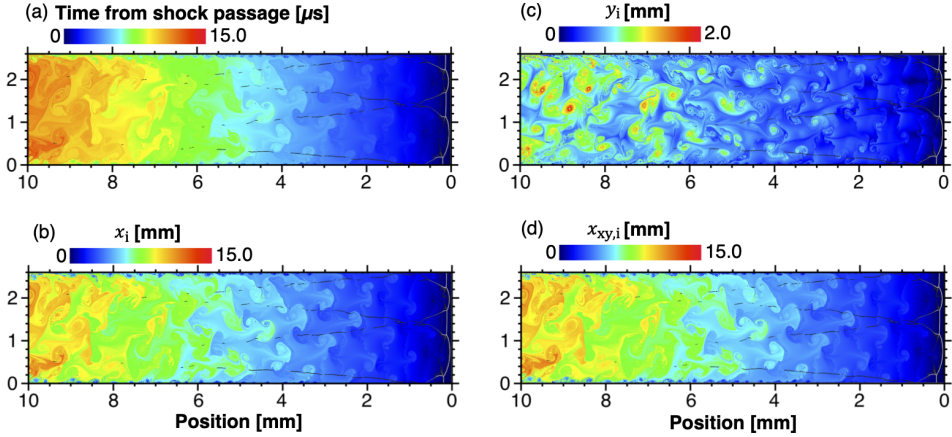


Figure 4: 2D instantaneous Lagrangian flow fields in $2\text{H}_2-\text{O}_2-7\text{Ar}$ mixture, superimposed with Schlieren density. (a) Time from shock passage; (b) longitudinal distance traveled by the Lagrangian particle x_i , (c) transverse distance traveled by the Lagrangian particle y_i , (d) distance traveled by the Lagrangian particle $x_{xy,i}$.

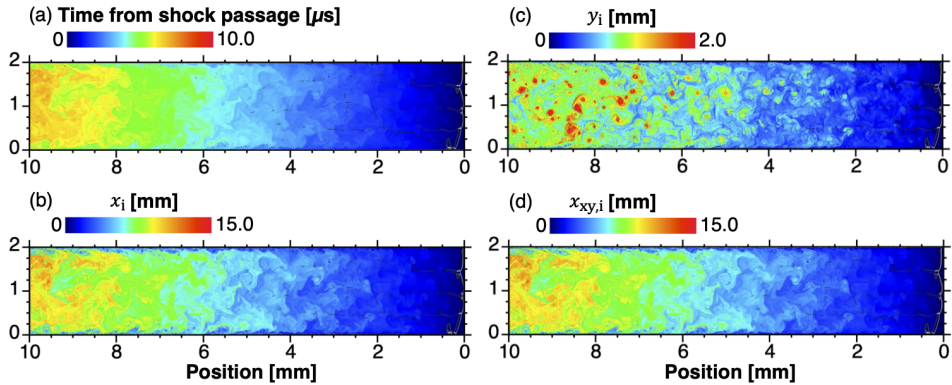


Figure 5: 2D instantaneous Lagrangian flow fields in $2\text{H}_2-\text{O}_2$ mixture, superimposed with Schlieren density. (a) Time from shock passage; (b) longitudinal distance traveled by the Lagrangian particle x_i , (c) transverse distance traveled by the Lagrangian particle y_i , (d) distance traveled by the Lagrangian particle $x_{xy,i}$.

409 entrained in the x -direction. The longitudinal distance x_i for the particles inside the boundary
 410 layer can also be seen to be shorter than that of the other particles in the core of the flow.

411 In order to compare the distribution of the distances for both mixtures, the average
 412 longitudinal distance \bar{x}_i is shown in Fig. 6. The slopes are different due to the difference
 413 in the velocity induced by detonation of both mixtures. The standard deviation for x_i (see
 414 Fig. 7(a)) $[\sum_i^N (x_i - \bar{x}_i)^2 / N]^{1/2}$ were almost the same. The average transverse distance \bar{y}_i (see
 415 Fig. 7(b)) can be as high as twice for the non-diluted as compared to the more stable case.

416 Figures 8(a,b) and 9(a,b) depict the joint pdf between the times from shock passage and the
 417 longitudinal and transverse distances traveled by the particles. The width of the distributions
 418 became wider as the time from shock passage increased. The fluctuations along the transverse
 419 distance y_i also increased (see Figs. 8(d) and 9(d)). From Figs. 8(c,d) and 9(c,d), the peak
 420 of the pdf for the fluctuations along the longitudinal direction was lower than that of the
 421 transverse direction, meaning that the dispersion along the longitudinal direction was greater
 422 than that of the transverse one. This finding that the dispersion along the longitudinal direction

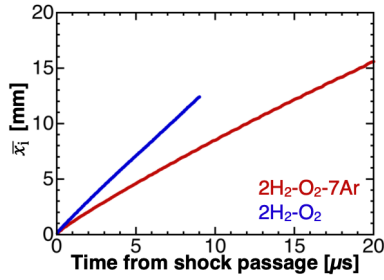


Figure 6: Average longitudinal distance \bar{x}_i for $2\text{H}_2-\text{O}_2-7\text{Ar}$ and $2\text{H}_2-\text{O}_2$ mixtures.

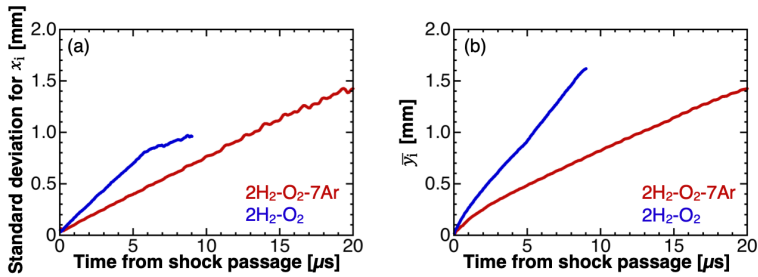


Figure 7: (a) Standard deviation for the longitudinal distance $[\sum_i^N (x_i - \bar{x}_i)^2 / N]^{1/2}$ and (b) average transverse distance \bar{y}_i for $2\text{H}_2-\text{O}_2-7\text{Ar}$ and $2\text{H}_2-\text{O}_2$ mixtures.

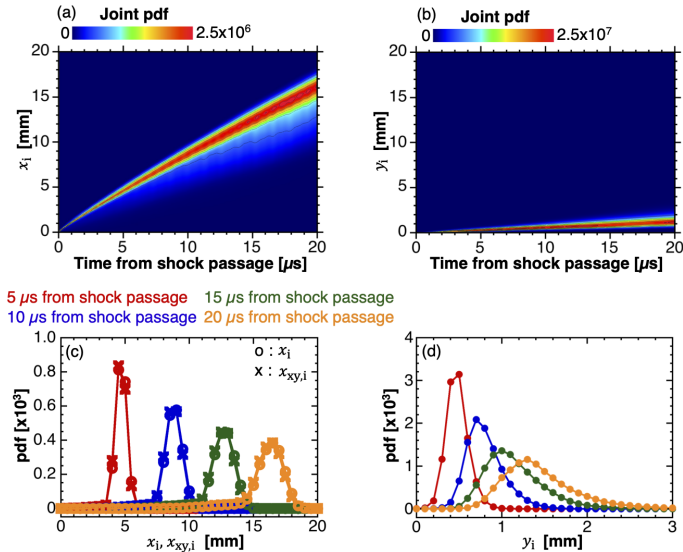


Figure 8: $2\text{H}_2-\text{O}_2-7\text{Ar}$ mixture. Joint pdf between (a) times from shock passage and longitudinal distances x_i , (b) times from shock passage and transverse distances y_i . Pdf at different instants for (c) longitudinal distances x_i and distances $x_{xy,i}$, (d) transverse distances y_i .

423 was greater than that of the transverse wave was not what could be expected from the presence
 424 of the transverse waves, characteristics and cornerstones of the detonation cellular structure.
 425 Moreover, the comparison of Figs. 8(c,d) and 9(c,d) showed that the diluted case needed
 426 about five times more time to obtain the same level of dispersion than the non-diluted one.

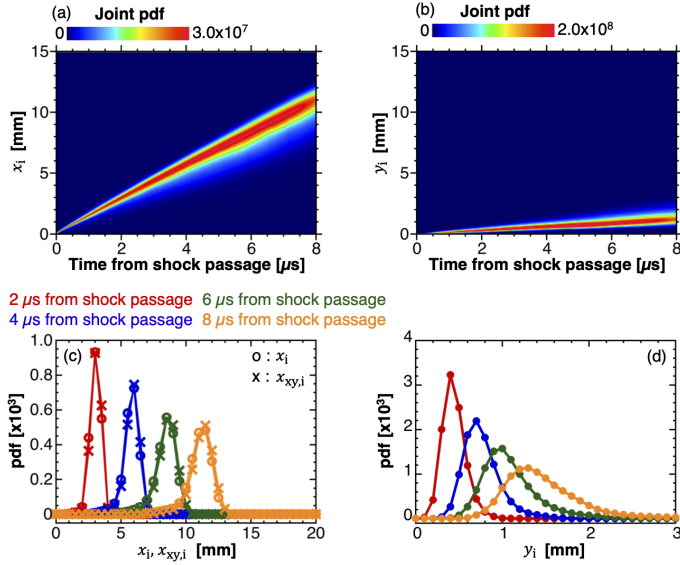


Figure 9: $2\text{H}_2\text{-O}_2$ mixture. Joint pdf between (a) times from shock passage and longitudinal distances x_i , (b) times from shock passage and transverse distances γ_i . Pdf at different instants for (c) longitudinal distances x_i and distances $x_{xy,i}$, (d) transverse distances γ_i .

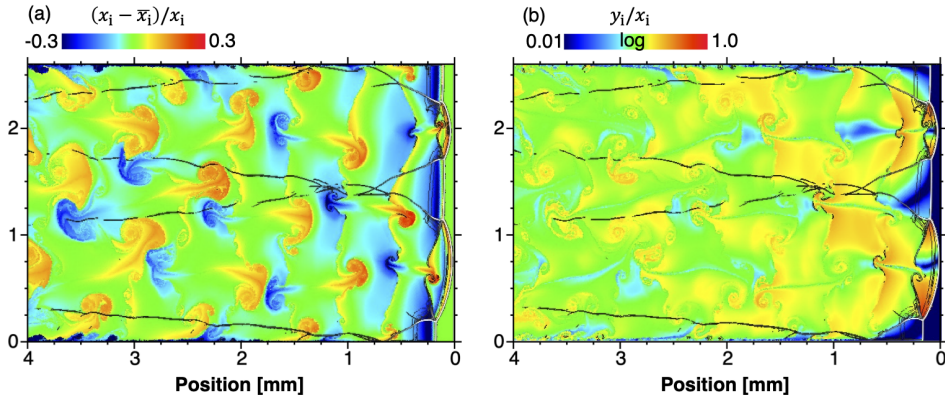


Figure 10: Diluted $2\text{H}_2\text{-O}_2\text{-7Ar}$ mixture. 2D instantaneous Lagrangian flow fields, superimposed with Schlieren density in diluted $2\text{H}_2\text{-O}_2\text{-7Ar}$ mixture. (a) Normalized fluctuations of the longitudinal distances $(x_i - \bar{x}_i)/x_i$, (b) normalized transverse distance γ_i/x_i .

427 Indeed, the average transverse distance $\bar{\gamma}_i$ became about one cell width after $17.8\ \mu\text{s}$ for the
 428 argon diluted case as compared to $3.6\ \mu\text{s}$ for the other case (Fig. 7(b)).

429 The 2D instantaneous Lagrangian flow fields of the normalized fluctuations in the
 430 longitudinal distance ($\delta x_i = (x_i - \bar{x}_i)/x_i$) and the normalized transverse distance γ_i/x_i have
 431 been plotted in Figs. 10 and 11 for both cases. Near the front, they came mainly from three
 432 factors. At first, the triple point collision resulted in forward jets with positive δx_i and in
 433 backward jets with negative values. Second, the decaying incident shock in the second part
 434 of the cell induced negative values. Finally, the transverse waves and the vortical motions
 435 played a major role in increasing γ_i , the more important contribution coming from the

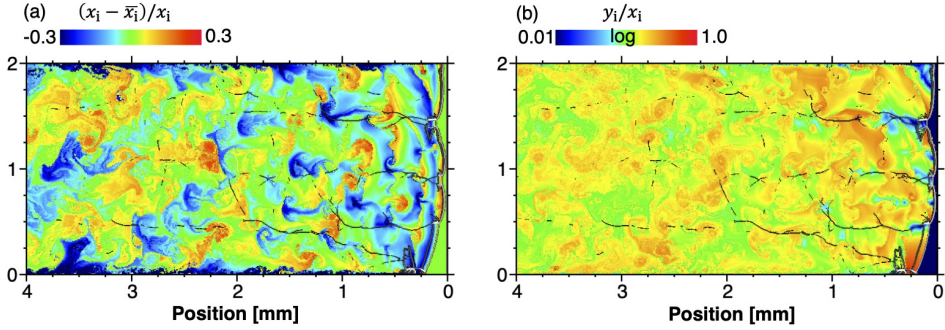


Figure 11: Non-diluted $2\text{H}_2 - \text{O}_2$ mixture. 2D instantaneous Lagrangian flow fields, superimposed with Schlieren density in diluted $2\text{H}_2 - \text{O}_2 - 7\text{Ar}$ mixture. (a) Normalized fluctuations of the longitudinal distances $(x_i - \bar{x}_i)/x_i$, (b) normalized transverse distance y_i/x_i .

436 latter, as time passed. Some differences were also present for δx_i near the boundary layer.
 437 The fluctuations appeared more spotty in the more unstable non-diluted case, with vortical
 438 motions also playing a more stronger role in the unstable case.

439

440 Figure 12 shows the time history of the variances of the x - and y - displacements $\overline{x_i'^2}$ and
 441 $\overline{y_i'^2}$, as well as their correlation $\overline{x_i' \cdot y_i'}$, which can be evaluated by Eqs. 4.1,4.2,4.3.

$$442 \quad \overline{x_i'^2} = \frac{1}{N} \sum_{i=1}^N \left[(x_{p,i} - x_{p,i,0}) - \overline{(x_{p,i} - x_{p,i,0})} \right]^2 = \frac{1}{N} \sum_{i=1}^N (x_i - \bar{x}_i)^2 \quad (4.1)$$

$$443 \quad \overline{y_i'^2} = \frac{1}{N} \sum_{i=1}^N (y_{p,i} - y_{p,i,0})^2 \quad (4.2)$$

$$444 \quad \overline{x_i' \cdot y_i'} = \frac{1}{N} \sum_{i=1}^N \left[(x_{p,i} - x_{p,i,0}) - \overline{(x_{p,i} - x_{p,i,0})} \right] \cdot (y_{p,i} - y_{p,i,0}) \quad (4.3)$$

445

446 Here, $x_{p,i,0}$ and $y_{p,i,0}$ are x and y initial positions of the particle i , and N is the number of
 447 particles.

448 The levels of fluctuations of the displacements $\overline{x_i'^2}$ and $\overline{y_i'^2}$ were much higher, about twice
 449 in the more irregular case (see Fig. 12(a)). As shown previously, the fluctuations in x_i and
 450 y_i increased as we move away from the shock (Figs. 10 and 11). The cross relation $\overline{x_i' \cdot y_i'}$
 451 oscillated around zero (see Fig. 12(c)). Indeed, the leading shock is curved and thus, for some
 452 positive positive y -displacements at some locations, there will be corresponding negative y -
 453 displacements at other locations. Moreover, in 2D, for each vortex rotating clockwise, there is
 454 another vortex rotating anti-clockwise. Near the leading shock, the fluctuations of transverse
 455 displacements were about that of the longitudinal ones (see Fig. 12(b)). Then the y -levels
 456 decreased comparatively. Thus, far from the shock, the flow became anisotropic. In 2D
 457 flows investigated, there lacks the vorticity stretching mechanism that would help to return
 458 more rapidly to isotropy (see Taieb (2020)). The good collapse of the curves in Fig. 12(d)
 459 suggested that a characteristic time scale was the induction time τ_{ind} and that a characteristic
 460 length scale was the induction length times the reduced activation energy $E_a/(RT_{vN}) \cdot x_{\text{ind}}$.
 461 This scaling used for the fluctuations of x -displacement as a function of the time from the
 462 shock passage is consistent with asymptotic studies (Buckmaster 1989; Lee 2008; Faria

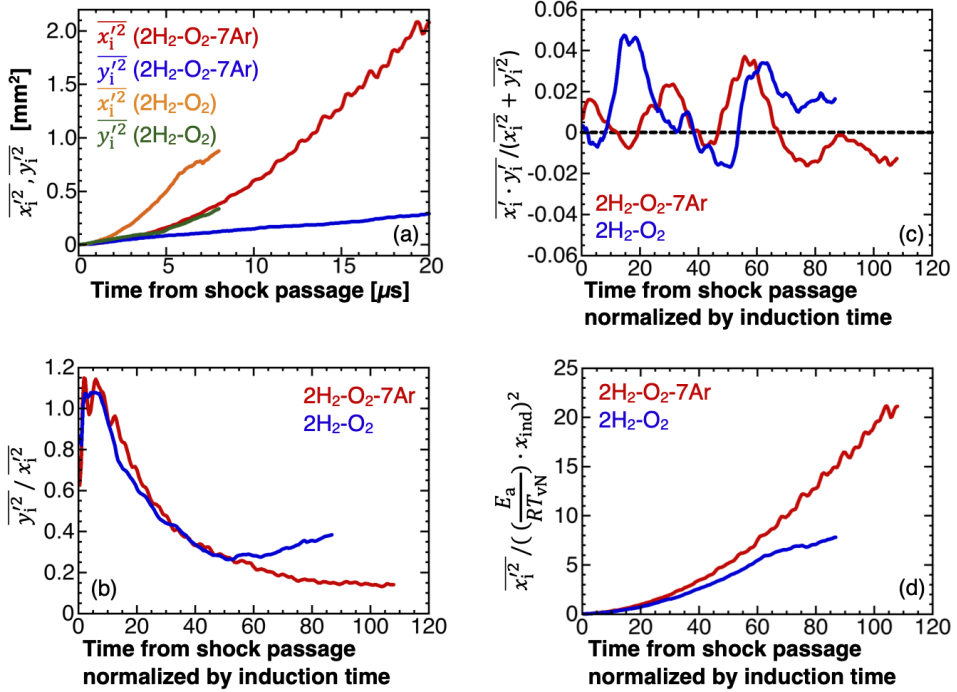


Figure 12: (a) Time history of the variance of the x - and y - displacements, $\overline{x_i'^2}$ and $\overline{y_i'^2}$, (b) nondimensionalized y - displacements, $\overline{y_i'^2} / \overline{x_i'^2}$ as a function of the nondimensionalized time τ / τ_{ind} , (c) $\overline{x_i' \cdot y_i'} / (\overline{x_i'^2} + \overline{y_i'^2})$, (d) nondimensionalized x - displacements, $\overline{x_i'^2} / ((\frac{E_a}{RT_{VN}}) \cdot x_{ind})^2$ as a function of the nondimensionalized time τ / τ_{ind} .

463 2014) even if the same characteristic length seemed to hold also for the transverse fluctuations
 464 in the present study.

465

4.2. Dispersion in induction time scale

466 The dispersion was studied in this subsection within the induction time scale and was related
 467 to the cellular structure.

468 The time sequence of the dispersion in term of the distance traveled by the Lagrangian
 469 particle from shock passage for 2H₂-O₂-7Ar and 2H₂-O₂ mixtures are depicted in Figs. 13
 470 and 14, respectively. Only the Lagrangian particles whose time from shock passage is less
 471 than the induction time are displayed. When the induction time was longer, the distance
 472 traveled $x_{xy,i}$ which is only shown within the induction time scale was longer.

473 In 2H₂-O₂-7Ar mixture, the first observation is that the induction process was completed
 474 within first half of one cell cycle (Fig. 13). The induction length was shorter behind the Mach
 475 stem in the first part of the cell and longer behind the decaying incident shock front in the
 476 second part of the cell. After the collision of the transverse waves, the Lagrangian particles,
 477 which passed the weaker incident shock completed the induction process. The dispersion
 478 was slightly deviated from the straight line parallel to the propagation direction due to the
 479 curved leading shock front (Mölder 2016).

480 In 2H₂-O₂ mixture, more variation in the induction time behind the leading shock front
 481 was observed due to higher reduced activation energy (Fig. 14). The distance in the unburned

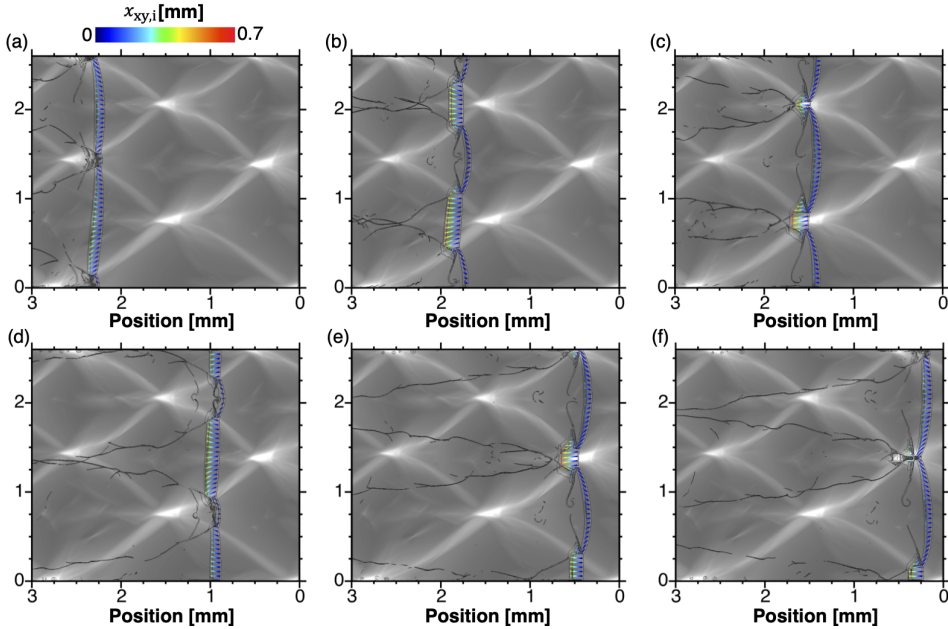


Figure 13: Time sequence of instantaneous 2D flow fields of distance traveled from shock passage $x_{xy,i}$ in $2\text{H}_2\text{-O}_2\text{-7Ar}$ mixture. Only the Lagrangian particles whose time from shock passage is less than the induction time are displayed. The Lagrangian particles selected for the display were separated by an initial vertical distance of $50\ \mu\text{m}$. The lines are the density Schlieren and the gray contour in the background is the maximum pressure. The detonation propagated from the left to the right and the time passed from (a) to (f).

482 gas pocket torn from the front was also much longer (see Fig. 14(c,e)). The leading shock
 483 curvatures were also higher, inducing more deviation.

484 In both cases, within the induction time scale, the transverse dispersion was mainly due
 485 to the curvature of the leading shock. This effect was more pronounced near the edges of
 486 the cell and during the first part of the cell, when the leading detonation front was a Mach stem.
 487

488 To relate the dispersion with the geometry of the cellular structure, the distance traveled
 489 by the Lagrangian particle and the normalized number density of Lagrangian particles α_L
 490 were shown in the position where they recorded their maximum thermicity (see Figs. 15 and
 491 16). Note that the number density was the projection of Lagrangian data over the Eulerian
 492 grid, with a spacing five times greater than the minimum grid width. The number density
 493 was then normalized by its initial value at its initial position to obtain α_L (see Eq. 4.4).

$$494 \quad \alpha_L = \frac{N_i}{N_{i,0}}, \quad (4.4)$$

495 where N_i and $N_{i,0}$ are the number of the Lagrangian particles, which are located on the
 496 Eulerian grid used for the projection and the number of the Lagrangian particles in the initial
 497 condition, respectively. The estimation of other variables on the Eulerian grid, such as the
 498 distance traveled by Lagrangian particles was done by the same projection over a box of
 499 width five times the grid cell size (see Eq. 4.5).

$$500 \quad \overline{\Phi_L} = \frac{\sum_{k=1}^{N_i} \Phi_{L,k}}{N_i} \quad (4.5)$$

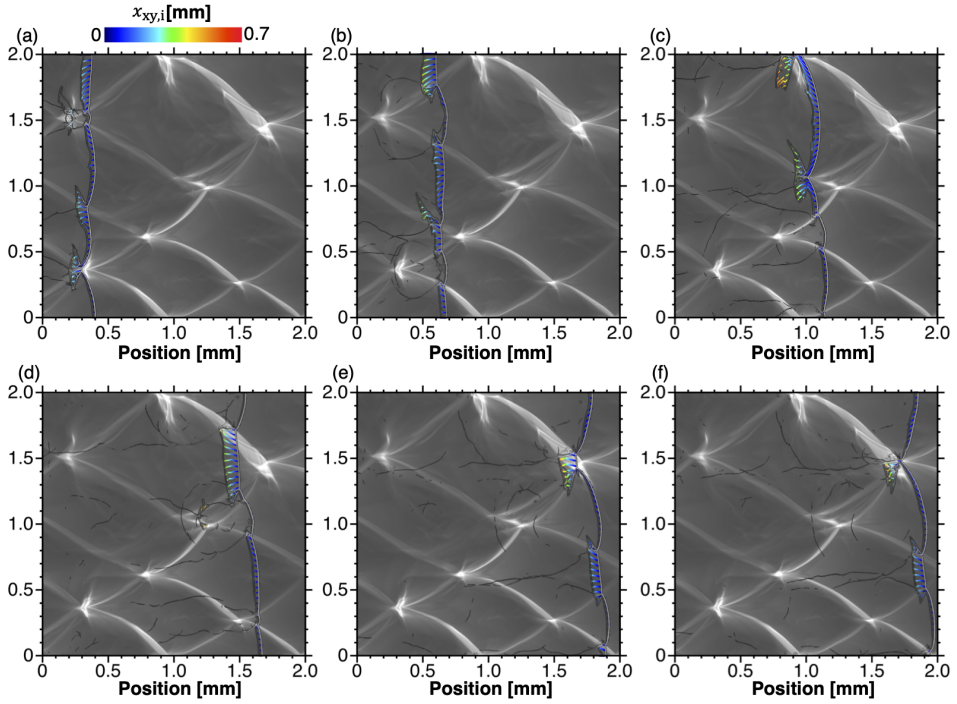


Figure 14: Time sequence of instantaneous 2D flow fields of distance traveled from shock passage $x_{xy,i}$ in $2\text{H}_2\text{-O}_2$ mixture. Only the Lagrangian particles whose time from shock passage is less than the induction time are displayed. The Lagrangian particles selected for the display were separated by an initial vertical distance of $40\ \mu\text{m}$. The lines are the density Schlieren and the gray contour in the background is the maximum pressure. The detonation propagated from the left to the right and the time passed from (a) to (f).

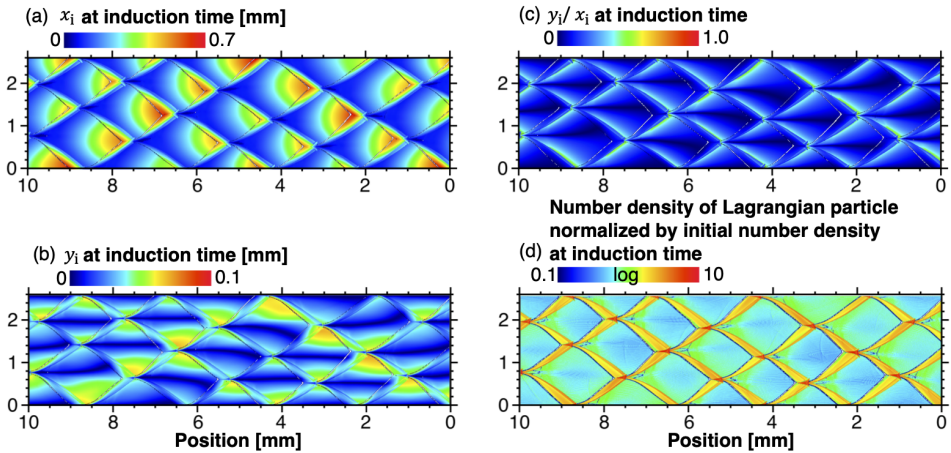


Figure 15: 2D flow fields of the projected Lagrangian values in the position where the Lagrangian particles experienced the maximum thermicity in $2\text{H}_2\text{-O}_2\text{-7Ar}$ mixture. (a) Projected longitudinal distance traveled x_i at the induction time, (b) projected transverse distance traveled $y_{x,i}$ at the induction time, (c) ratio of transverse distance to longitudinal distance y_i/x_i at induction time, (d) number density of Lagrangian particles normalized by the initial number density. The displayed region is the same as in Fig. 2. The region where no Lagrangian particle was located was displayed as white color.

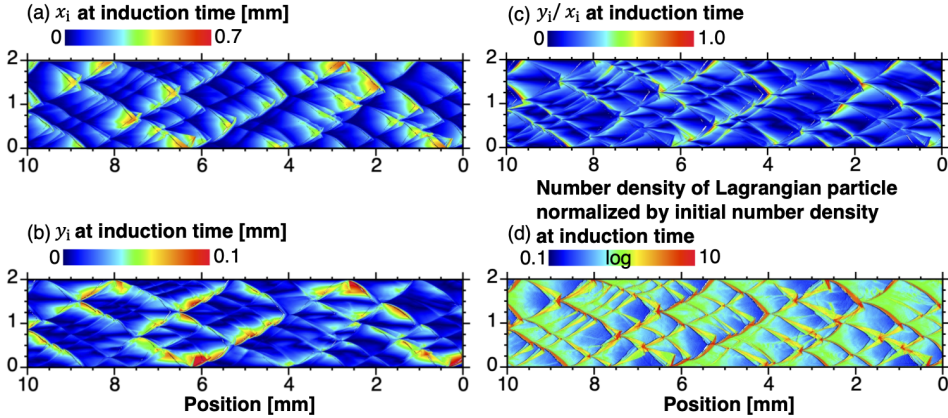


Figure 16: 2D flow fields of the projected Lagrangian values in the position where the Lagrangian particles experienced the maximum thermicity in 2H₂-O₂ mixture. (a) Projected longitudinal distance traveled x_i at the induction time, (b) Projected transverse distance traveled y_i at the induction time, (c) ratio of transverse distance to longitudinal distance y_i/x_i at induction time, (d) number density of Lagrangian particles normalized by the initial number density. The displayed region is the same as in Fig. 3. The region where no Lagrangian particle was located was displayed as white color.

501 Here, $\overline{\Phi_L}$ and $\Phi_{L,k}$ are the projected Lagrangian value and the Lagrangian value for the k^{th}
 502 Lagrangian particle, which were located on the Eulerian grid, respectively. The distributions
 503 of the distance traveled by Lagrangian particle and the number density at the induction time
 504 can be seen to be closely related to the cellular structure (see Figs. 15, 16, 2(c), 3(c)). There are
 505 regions in the cellular structure where the Lagrangian particles did not complete the induction
 506 process (Figs. 15, 16). From the instantaneous flow fields, these regions were seen to be thin
 507 non-reactive tails in the gas between the leading shock front and the transverse waves due
 508 to the lower temperature, which were reported numerically by Gamezo et al. (2000) and
 509 observed experimentally by Xiao and Radulescu (2020) in hydrogen-oxygen-argon mixture.
 510 The longitudinal distance x_i tended to be larger at the end of the cell (Figs. 15(a), 16(a)), due to
 511 the decaying shock wave. Near the edge of the cells, the transverse distance y_i was comparable
 512 to the longitudinal distance traveled x_i , due to the transverse waves. (Figs. 15(b), 16(b)). The
 513 ratio y_i/x_i was also the highest near edges (Figs. 15(c), 16(c)), and increased as the mixture
 514 became more unstable. This ratio was also minimum at the centerline of the cell.

515 The propagation of the cellular detonation dispersed the Lagrangian particles and their
 516 distribution was non uniform (Figs. 15(d), 16(d)). The Lagrangian particles were locally
 517 accumulated the trajectory of the triple points. Less Lagrangian particles were found inside
 518 the cells.

519 In the weakly unstable 2H₂-O₂-7Ar mixture, the number density of Lagrangian particles
 520 was the highest between the collision of the transverse waves and the triple point collision.
 521 The accumulation of Lagrangian particles at the collision point of the transverse waves gave
 522 birth to the local explosion, of which induced blast waves driving the cellular structure, as
 523 modeled by Vasilev and Nikolaev (1978) and Crane et al. (2021).

524 In addition, there were some differences in the simulation results. The transverse waves
 525 accumulated the Lagrangian particles along the the triple point trajectory and the other
 526 particles completed the induction process inside the cell in the simulation. This observation
 527 was in line with the previous analysis by Strehlow (1970) that the major source of the
 528 energy that produced the blast wave came from the transverse shock waves. As the mixture
 529 instability increased, the contribution of the transverse waves in the accumulation of the

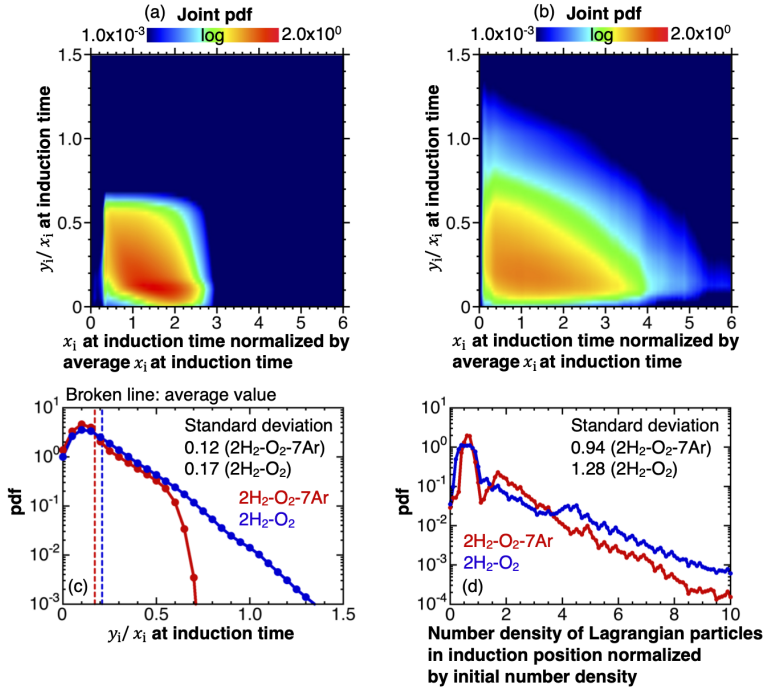


Figure 17: Pdf for the values at the induction time. (a) Joint pdf between normalized x_i/\hat{x}_i and y_i/x_i in 2H₂-O₂-7Ar mixture, (b) joint pdf between normalized x_i/\hat{x}_i and y_i/x_i in 2H₂-O₂ mixture, (c) pdf for y_i/x_i , (d) pdf for normalized number density. \hat{x}_i is the average of x_i at induction time over the whole computational domain.

530 Lagrangian particles experiencing the maximum thermicity increased (Figs. 15(d),16(d)). In
 531 the 2H₂-O₂ mixture, some of the strong transverse waves accumulated the particles along
 532 the triple point trajectories at the same level as near the transverse wave collision. In addition,
 533 the normalized number density can become locally higher as compared to the highest values
 534 of the diluted case.

535 The differences between the physical picture of the model (Vasilev and Nikolaev 1978;
 536 Crane et al. 2021) and the simulation results were more apparent in 2H₂-O₂ mixture than
 537 in 2H₂-O₂-7Ar mixture. These additional features on the accumulation and the dispersion
 538 of the Lagrangian particles in the induction time scale revealed in this study can provide
 539 guidelines for the development of a model for the prediction of the cellular structure and
 540 their size.

541 The pdf for the values at the induction time were depicted in Fig. 17. The distribution of
 542 normalized x_i at the induction time became wider as the mixture instability increased due
 543 to the variation of the induction time behind cellular detonation front by the higher reduced
 544 activation energy and the presence of unburned gas pockets (Figs. 17(a,b)). The distribution
 545 of y_i/x_i was also wider and its average value was larger for the non diluted mixture, due to
 546 stronger transverse waves (Figs. 17(a,b,c)). High values of y_i/x_i with small x_i could be found
 547 around the triple point trajectories, due to stronger transverse motion by stronger transverse
 548 waves (Figs. 15(c),16(c),17(a,b)). As x_i increased, y_i/x_i decreased (see Figs. 12(b),17(a,b)).

549 The peak for distribution of y_i/x_i at the induction time was located around 0.1 (Fig. 17(c))
 550 and the deviation of the trajectories of particles from the straight line in the induction time
 551 scale was not large, as seen in Figs. 13,14. The pdf for the normalized number density of
 552 Lagrangian particles is depicted in Fig. 17(d). It had three and two peaks for diluted and

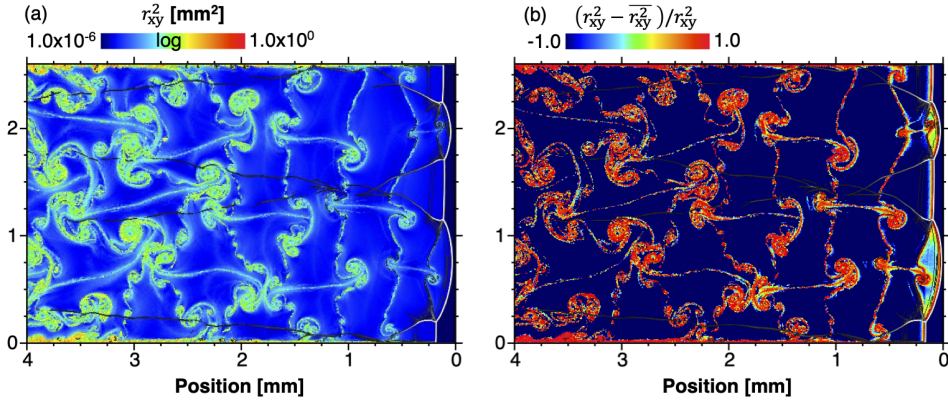


Figure 18: Diluted 2H₂-O₂-7 Ar mixture. 2D instantaneous Lagrangian flow fields, superimposed with Schlieren density. (a) Square of the relative dispersion r_{xy}^2 , (b) normalized fluctuation of the square of the relative dispersion $(r_{xy}^2 - \overline{r_{xy}^2})/r_{xy}^2$.

553 non diluted cases, respectively. For the diluted case, the first peak corresponded to particles
 554 inside the cell, which were the most and which are in the dilute side (values lower than one).
 555 The second peak corresponded to the trajectories of the triple points and the third one to the
 556 locations between the collisions of the transverse waves and of the triple points. These two
 557 latter peaks are in the dense side (values greater than one). For the non diluted case, only
 558 two peaks can be highlighted. The first peak corresponded to the particles inside the cell,
 559 as in the diluted case. The second peak corresponded more or less to a merge between the
 560 second and third peaks of the diluted case.

561

562 The results in Sections 4.1 and 4.2 highlighted that the dispersion of the Lagrangian
 563 particles was promoted behind the detonation front. The fact that the scaling for the variance
 564 of the x -displacement $\overline{x_1^2}$ worked well using $E_a/(RT_{vN}) \cdot x_{ind}$ suggested that the dispersion
 565 mainly came from an one-dimensional instability mechanism (Fig. 12(d)), mainly due to the
 566 pulsations of the leading shock.

567 The curvature of the leading shock front was responsible for the transverse dispersion of
 568 the particles (Mölder 2016), deviating the particles from horizontal detonation propagation
 569 direction (Figs. 13 and 14). Moreover, another source of transverse dispersion came from
 570 the presence of the reaction front. The value of $\overline{y_1^2}/\overline{x_1^2}$ was maximum around $2\tau_{ind}$ in the
 571 simulation results, which was indicative that the dispersion in transverse direction increased
 572 around the reaction front (Fig. 12(b)). Indeed, Buckmaster and Ludford (1986) showed in a
 573 study on linear stability of steady, plane, overdriven detonation that the transverse velocity
 574 arose from the transverse derivative of the horizontal distance between the locations of the
 575 leading shock and the reaction front. Transverse waves clearly contributed to increase these
 576 effects (Emmons 1958).

577 In addition, jets induced fluctuations in the longitudinal dispersion (Figs. 10 and 11). The
 578 role of the jets on the fluctuations in the dispersion are expected to become more important
 579 for mixtures with lower isentropic coefficient at vN state (Lau-Chapdelaine et al. 2021; Sow
 580 et al. 2021; Taileb et al. 2021).

581

4.3. Relative dispersion

582 The dispersion behind the front was further evaluated in terms of the relative dispersion in
 583 this subsection. The initial distance between two Lagrangian particles in the same pair was

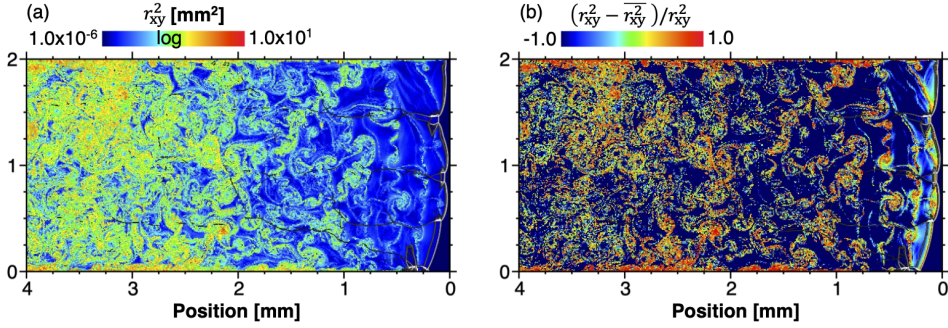


Figure 19: Non-diluted $2\text{H}_2\text{-O}_2$ mixture. 2D instantaneous Lagrangian flow fields, superimposed with Schlieren density. (a) Square of the relative dispersion r_{xy}^2 , (b) normalized fluctuation of the square of the relative dispersion $(r_{xy}^2 - \overline{r_{xy}^2})/r_{xy}^2$.

584 set to be the grid size upstream of the leading front, which is the minimum grid width. To
 585 distinguish the relative dispersion in the longitudinal and transverse directions, the following
 586 relative dispersion were evaluated:

$$587 \quad r_{xy} = \left[(x_{p,i1} - x_{p,i2})^2 + (y_{p,i1} - y_{p,i2})^2 \right]^{1/2} \quad (4.6)$$

$$588 \quad r_x = |x_{p,i1} - x_{p,i2}| \quad (4.7)$$

$$589 \quad r_y = |y_{p,i1} - y_{p,i2}| \quad (4.8)$$

591 Here, $x_{p,i1}$ and $y_{p,i1}$ are x and y positions of the particle $i1$, and $x_{p,i2}$ and $y_{p,i2}$ are x and y
 592 position of the particle $i2$ which forms the pair with particle $i1$.

593 The 2D Lagrangian instantaneous flow fields for the relative dispersion for both mixtures
 594 are shown in Figs. 18 and 19. The relative dispersion $\overline{r_{xy}^2}$ was the average value at the time
 595 from shock passage. The displayed value of r_{xy}^2 for each particle was the value averaged over its
 596 four pairs. Two main factors contributed to the highest values. First, the particles with higher
 597 relative dispersion experienced the shear layers emanating from the triple shock interaction
 598 and their curling to form the large scale turbulent eddies. The second factor came from the
 599 presence of the boundary layer due to the velocity gradient. The normalized deviation from
 600 the average $(r_{xy}^2 - \overline{r_{xy}^2})/r_{xy}^2$ highlighted these two main contributions (Figs. 18(b)19(b)). The
 601 relative dispersion was higher for the irregular mixture (Figs. 18(a)19(a)), with particles with
 602 higher relative dispersion being more dispersed inside the channel.

603 Figure 20 shows the square of average relative dispersion for $2\text{H}_2\text{-O}_2\text{-7Ar}$ and $2\text{H}_2\text{-O}_2$
 604 mixtures. The Lagrangian Favre average used for Fig. 20(d) based on the time from shock
 605 passage is described in next subsection 4.4. In both mixtures, the average of r_x is higher than
 606 of r_y , highlighting again the anisotropy downstream the leading front (Fig. 20(a)).

607 After some time, corresponding to some μs and far from the leading shock, a self-similar
 608 behavior for both mixtures was found when the mean relative dispersion $\overline{r_{xy}}$ was scaled by
 609 the characteristic length scale $\chi \cdot x_{\text{ind}}$. The $E_a/(RT_{\text{VN}}) \cdot x_{\text{ind}}$ length scale used in Section
 610 4.1 was not found to give nice results. Indeed, the relative dispersion of nearby particles is
 611 related to their difference of velocities that could be a result of the acceleration of reactive
 612 fronts, which is reflected by the nondimensionalized acceleration parameter χ (Sharpe 2002;
 613 Radulescu et al. 2013; Tang and Radulescu 2013). Moreover, compensated by $(\tau/\tau_{\text{ind}})^3$, the
 614 nondimensionalized pair dispersion from Fig. 20(c) agreed with the Richardson-Obukhov
 615 (R-O) law (Richardson 1926; Salazar and Collins 2009), meaning that $(r_{xy}/(\chi \cdot x_{\text{ind}}))^2$

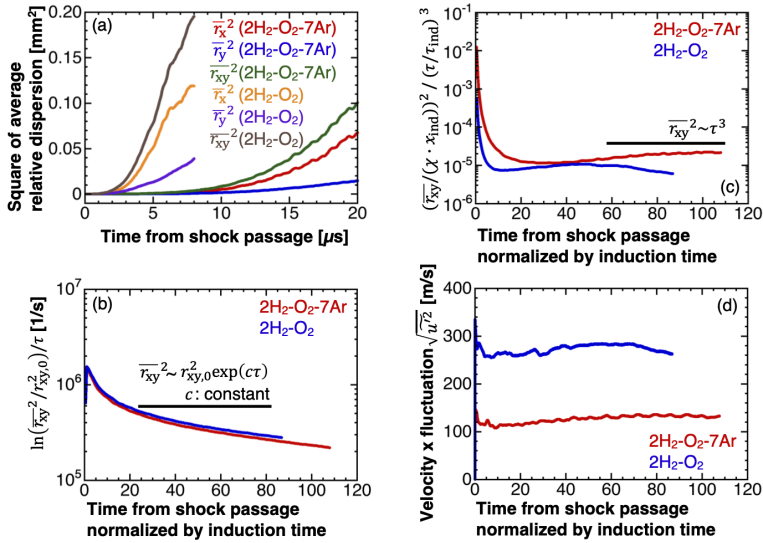


Figure 20: Time history of the average relative dispersion for 2H₂-O₂-7Ar and 2H₂-O₂ mixtures. (a) Square of average relative dispersion $\overline{r_x^2}$, $\overline{r_y^2}$, $\overline{r_{xy}^2}$, as a function of time passage τ , (b) logarithm of $\overline{r_{xy}^2}/r_{xy,0}^2$ compensated by τ , (c) time history of normalized $(\overline{r_{xy}^2}/(\chi \cdot x_{ind}))^2$ compensated by normalized $(\tau/\tau_{ind})^3$, (d) x -velocity fluctuations $\sqrt{u'^2}$. $r_{xy,0}$ is the initial value for r_{xy} .

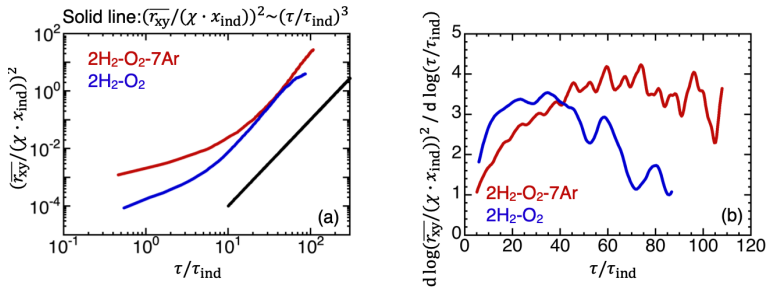


Figure 21: 2H₂-O₂-7Ar and 2H₂-O₂ mixtures. (a) Time evolution of $(\overline{r_{xy}^2}/(\chi \cdot x_{ind}))^2$, (b) local scaling exponent of $\overline{r_{xy}^2}$ from $d[\log(\overline{r_{xy}^2}/(\chi \cdot x_{ind}))^2] / d[\log(\tau/\tau_{ind})]$.

616 scaled as $\sim (\tau/\tau_{ind})^3$. Darragh et al. (2021) in another context of high speed premixed flames
 617 also found such scalings within some range but with different scalings. The exponential time
 618 dependence for inert flow (Babiano et al. 1990) did not hold (see Fig. 20(b)) for the lower
 619 times, the constant spanning over more than one order of magnitude. Indeed, the latter zone
 620 was the zone of the main heat release (see Table 7).

621 Figure 21 indicates the derivative of the relative dispersion with respect to time. The local
 622 exponent value is 3.77 ($50 < \tau/\tau_{ind} < 80$) and 3.38 ($20 < \tau/\tau_{ind} < 40$) for the diluted and non
 623 diluted case, respectively. However, the nondimensionalized time τ/τ_{ind} corresponding to
 624 the hydrodynamic thickness for both mixtures was around 50 (see Table 7). Therefore, only
 625 the unstable case approached the R-O prediction within the detonation driving zone. The
 626 diluted case approached the R-O prediction only around the mean sonic surface. The initial
 627 distance in the stable case was larger than that in the unstable case, so the relaxation to the
 628 R-O scaling may also take longer (Bourgoin et al. 2006).

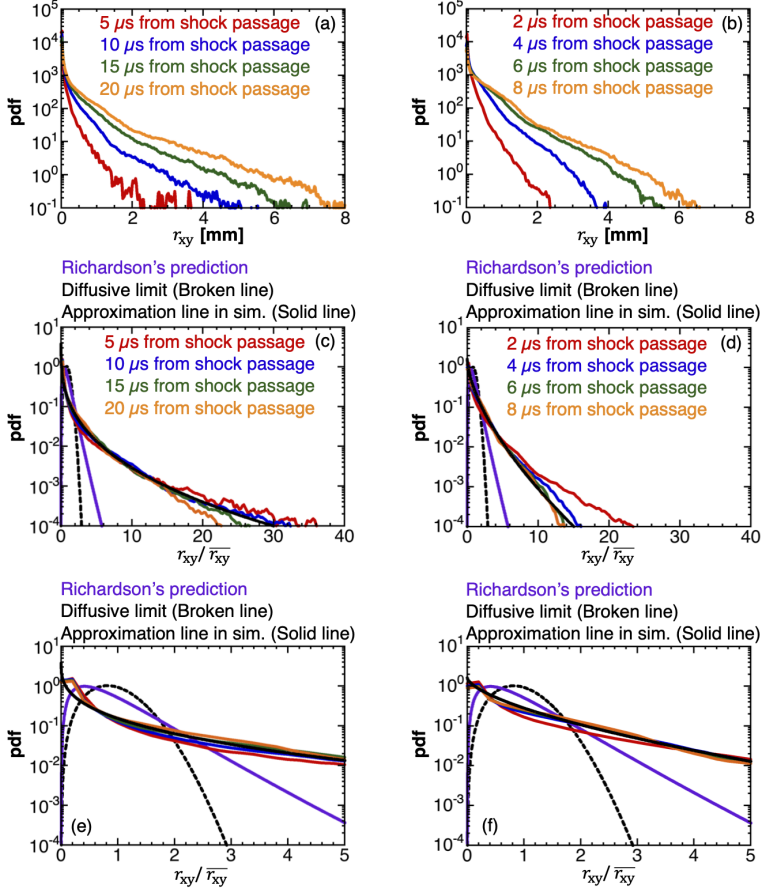


Figure 22: Left: $2\text{H}_2 - \text{O}_2 - 7\text{Ar}$ mixture. Right: $2\text{H}_2 - \text{O}_2$ mixture. (a,b) pdf for relative dispersion r_{xy} , (c,d) pdf for r_{xy}/\bar{r}_{xy} , (e,f) Enlarged view of pdf for r_{xy}/\bar{r}_{xy} .

Mixture	A	α	β
$2\text{H}_2 - \text{O}_2 - 7\text{Ar}$	3.78	3.21	0.35
$2\text{H}_2 - \text{O}_2$	1.63	1.76	0.63

Table 2: Coefficients of the function approaching the pdf of the normalized relative dispersion r_{xy}/\bar{r}_{xy} : $\text{pdf} = A \exp(-\alpha(r_{xy}/\bar{r}_{xy})^\beta)$ (Jullien et al. 1999). The Richardson's prediction gives $\beta = 2/3$.

629 The R-O law reads $r_{xy}^2/\tau^3 \sim \langle \epsilon \rangle$, with $\langle \epsilon \rangle$ being the turbulent energy dissipation
630 rate (Salazar and Collins 2009). One can thus estimate $\langle \epsilon \rangle \sim \langle \delta u \rangle^2 / \tau_{\text{ind}}$ as the ratio
631 between the square of the x -velocity fluctuations δu and an induction time τ_{ind} . From
632 Fig. 20(d), the ratio of the velocity fluctuations between the diluted and non-diluted
633 cases after the induction and reaction zones is about ~ 2 . Another estimation came from
634 the turbulent energy dissipation rates $\langle \delta u \rangle_{\text{non-diluted}} / \langle \delta u \rangle_{\text{diluted}} \sim [(\langle \epsilon \rangle_{\text{non-diluted}} / \langle \epsilon \rangle_{\text{diluted}} \times$
635 $\tau_{\text{ind, non-diluted}} / \tau_{\text{ind, diluted}})]^{1/2} \sim 3$. This very good correspondence from such rough estimates
636 seemed to indicate that after the main heat release zone, the more unstable the mixture was,
637 the more turbulent the flow can be considered to be.

638 To evaluate the distribution in the relative dispersion, the pdf for the relative dispersion
639 r_{xy} is depicted in Fig. 22 for the diluted and non-diluted mixtures, respectively. The curves
640 for the diffusive limit and the inertia regime were also included in Figs. 22(c,d,e,f) for
641 comparison. These equations are recalled in Appendix C. The distribution become wider as
642 the time from shock passage increased (Fig. 22(a,b)). The same levels of relative dispersion
643 was obtained much more rapidly in the non-diluted case. The relative dispersion is strongly
644 non-gaussian, with long tails developing, indicative of rare events. In Figs. 22(c,d,e,f), the
645 relative dispersion has been rescaled by $\overline{r_{xy}}$ and a reasonably good collapse of the curves
646 was obtained, showing that the process was self-similar in time, except for the rare events.
647 A good fit for the tails of the pdfs reads $A \exp(-\alpha(r_{xy}/\overline{r_{xy}})^\beta)$ (Jullien et al. 1999) and their
648 coefficients are given in Table 2. The exponent was about 0.35 and applied well for values of
649 $r_{xy}/\overline{r_{xy}}$ between 5 and 15 for the diluted mixture, and was about 0.63 for values of $r_{xy}/\overline{r_{xy}}$
650 between 2 and 8 for the non-diluted one. The exponent for the unstable case agreed very
651 well with the Richardson's proposal of $2/3$ (Richardson 1926) while that in the diluted case
652 was below the latter value. The normalized relative dispersion for the non-diluted was less
653 steeper and higher for the most probable events in the intermediate range (see values of the
654 fitted function in Table 2), consistent with the fact that the mixture was considered to be more
655 unstable near the leading shocks based on the reduced activation energy and χ parameters.
656 What was more surprising was the presence of very rare events with high levels of relative
657 dispersion for the diluted and regular case.

658 The probability of rare events was higher than that of the Richardson's prediction (Buaria
659 et al. 2015) (see Figs. 22(e)(f)). In the derivation of the pdf by Richardson, the dispersion
660 process was described by a diffusive equation. This modeling was based on two assump-
661 tions (Boffetta and Sokolov 2002). The first one is that the dispersion process was self-similar
662 in time. In our case, this assumption that the dispersion process was self-similar in time was
663 valid (see Figs. 22(c,d,e,f)). The second one was that the velocity field was short correlated
664 in time (Sokolov 1999). The relative velocity in quasi-Lagrangian coordinate (Boffetta et al.
665 1999) was then evaluated to check this validity of the latter assumption. The relative velocity
666 in quasi-Lagrangian coordinate $\mathbf{v}^{QL}(\mathbf{R}, \tau)$ at time from shock passage τ was defined by the
667 following equation.

$$668 \quad \mathbf{v}^{QL}(\mathbf{R}, \tau) = \mathbf{v}(\mathbf{r}_1(\tau) + \mathbf{R}, \tau) - \mathbf{v}(\mathbf{r}_1(\tau), \tau) \quad (4.9)$$

670 Here, $\mathbf{v}(\mathbf{r}, \tau)$ is the Eulerian velocity field (u, v) at the position \mathbf{r} and the time from shock
671 passage τ . The position of the Lagrangian particles at time from shock passage τ is $\mathbf{r}_1(\tau)$.
672 The separation distance is \mathbf{R} . Note that only the particles that have passed the shock were
673 taken into account. The velocities were obtained by interpolation of three nearby Eulerian
674 cells (Eq. 2.34).

675 The relative velocity in quasi-Lagrangian coordinate as a function of separation distance
676 for $2\text{H}_2\text{-O}_2\text{-7Ar}$ and $2\text{H}_2\text{-O}_2$ mixtures is shown in Fig. 23. When the separation distance was
677 greater than the induction length, $(\mathbf{v}^{QL}(\mathbf{R}, \tau))^2$ was constant. However, when the separation
678 distance was less than the induction length, regardless of the mixture regularity and time
679 from shock passage, the square of relative velocity in quasi-Lagrangian coordinate was
680 proportional to square of the separation distance, i.e. $(\mathbf{v}^{QL}(\mathbf{R}, \tau))^2 \propto (\mathbf{R}/x_{\text{ind}})^2$. This
681 exponent of 2 was much higher than the exponent of $2/3$, which is expected for the case
682 of the Kolmogorov turbulence. Therefore, the velocity field behind the detonation front was
683 not short time correlated. Thus, the dispersion process can not be described by the diffusive
684 equation proposed by Richardson. The probability of the rare event in the relative dispersion
685 was then different from the Richardson's prediction. In addition, the present finding that
686 the velocity field behind the detonation front was different from that in the Kolmogorov

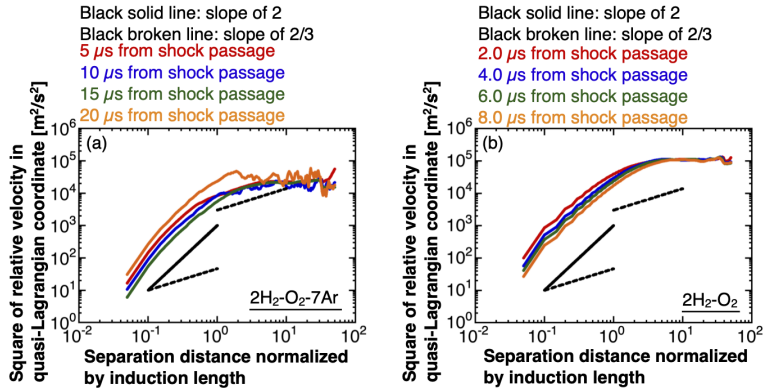


Figure 23: Square of relative velocity in quasi-Lagrangian coordinate as a function of separation distance normalized by induction length for various time from shock passage. (a) $2\text{H}_2-\text{O}_2-7\text{Ar}$ mixture, (b) $2\text{H}_2-\text{O}_2$ mixture. The black solid line is the curve with slope of 2 and the black broken line is the curve with slope of $2/3$.

687 turbulence can help to develop a turbulent model for detonation. Indeed, Maxwell et al.
 688 (2017) conducted numerical simulation with compressible linear eddy model for large-eddy
 689 simulation for the highly unstable mixture of methane-oxygen. They had to increase the
 690 Kolmogorov constant from the theoretical prediction for incompressible three-dimensional
 691 Kolmogorov turbulence to match the experimental results. In addition, in 2D simulations
 692 of the transition of a turbulent shock-flame complex to detonation, Maxwell et al. (2018)
 693 decreased this constant. These changes of the constant may come from the fact that the
 694 velocity field behind the detonation was not that of a Kolmogorov turbulence.

695 The fact that the velocities were not short correlated below the induction length, and
 696 that the relative dispersion scaled with χ parameter suggested that within the detonation
 697 driving zone, the heat release played a significant role. Indeed, $\chi = x_{\text{ind}}/x_{\text{reac}} \cdot E_a/(RT_{\text{vN}})$ (\approx
 698 $(T/x_{\text{reac}}) \cdot \partial x_{\text{ind}}/\partial T)_{\text{vN}}$) is related to the rather rapid energy deposition, which promotes the
 699 dispersion of the particles on the reaction length scale.

700 The other possible reason for the departure of the probability of the rare event in the relative
 701 dispersion from the Richardson's theory was the extreme events of pair separating much
 702 faster and slower than the average. Scatamacchia et al. (2012) reported in 3D incompressible
 703 homogeneous and isotropic turbulence that the extreme events making much faster pair
 704 separation and much slower pair separation than the average induced the deviation from the
 705 behavior in the Richardson's theory. The relative dispersion behind the detonation front was
 706 much higher than the average for the Lagrangian particles, which experienced the shear layers
 707 emanating from the triple shock interaction and which were located in the boundary layer.
 708 The other particles separated much slower (Figs. 18,19). The possible effect of the presence
 709 of slip lines and boundary layers (Figs. 18,19) on the higher possibility of the rare event
 710 was estimated by making pdf from the data with and without their presence. The criterion to
 711 distinguish the higher relative dispersion due to the slip lines and boundary layers was that
 712 the normalized fluctuation of the square of the relative dispersion $(r_{\text{xy}}^2 - \overline{r_{\text{xy}}^2})/r_{\text{xy}}^2$ was higher
 713 than -0.95.

714 To evaluate the distribution in the relative dispersion for the data with and without the
 715 presence of the slip lines and boundary layers, a new pdf for the normalized relative dispersion
 716 for the new set of data is depicted in Fig. 24. Regardless of the data based on the value of
 717 $(r_{\text{xy}}^2 - \overline{r_{\text{xy}}^2})/r_{\text{xy}}^2$, the shapes of the pdf were the same as in Figs. 22(e,f) and probability of the
 718 rare event in the relative dispersion remained higher than that from Richardson's theory. The

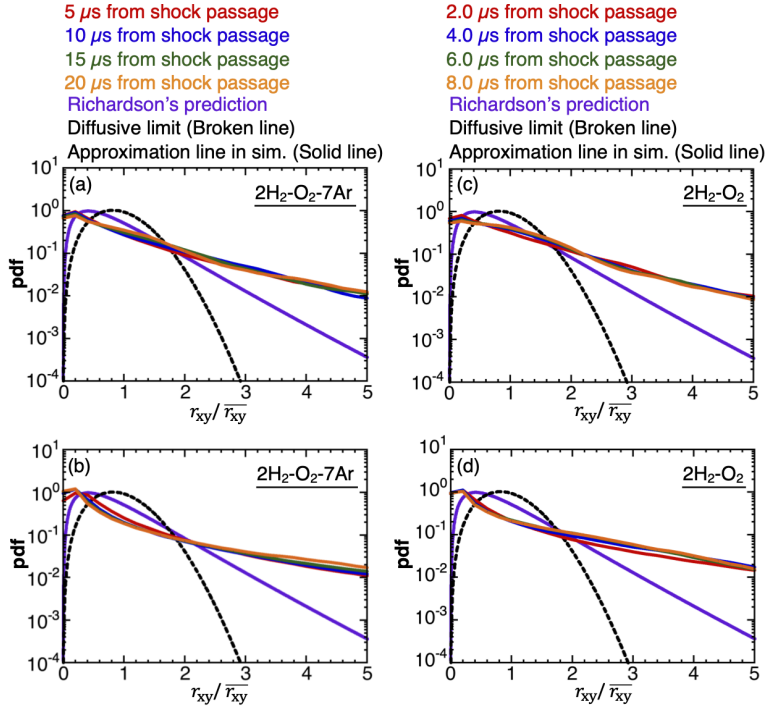


Figure 24: Pdf for r_{xy}/\bar{r}_{xy} from the categorized data (without slip lines and boundary layers) based on the value of $(r_{xy}^2 - \bar{r}_{xy}^2)/r_{xy}^2$. Left: $2\text{H}_2 - \text{O}_2 - 7\text{Ar}$ mixture. Right: $2\text{H}_2 - \text{O}_2$ mixture. (a,c) pdf for r_{xy}/\bar{r}_{xy} from the data whose $(r_{xy}^2 - \bar{r}_{xy}^2)/r_{xy}^2$ is higher than -0.95 , (b,d) pdf for r_{xy}/\bar{r}_{xy} from the data whose $(r_{xy}^2 - \bar{r}_{xy}^2)/r_{xy}^2$ is lower than -0.95 .

719 same conclusion was obtained if the threshold was changed from -0.95 to 0.95 (not shown
 720 here). Thus, the presence of the slip lines and boundary layers was not the main factor for the
 721 probability of rare events in the relative dispersion to be higher than that from Richardson's
 722 prediction in the flow field behind the detonation front.

723 Another possible reason for this difference in the pdf of the relative dispersion is that the
 724 turbulence has two cascades: an upward cascade coming from exothermic reactions and the
 725 downward Kolmogorov-like cascade (Radulescu 2003; Radulescu et al. 2005). In addition,
 726 the dispersion is slightly anisotropic in our 2D case (see Section 4.1), which can explain the
 727 deviations from results of isotropic turbulence (Xia et al. 2019). Moreover, the curves in the
 728 pdf in the simulation are different from that in the diffusive regime.

729

4.4. Eulerian and Lagrangian averaging procedures

730 As a result of the dispersion, the same distance from the mean leading shock can be reached
 731 by several Lagrangian particles at different times, traveling different distances. Figures 25
 732 and 26 depict the joint pdf between the longitudinal distance from the shock x_s and (a) the
 733 time from shock passage τ and (b) the distance traveled by the particle $x_{xy,i}$. The width of the
 734 distribution for τ and $x_{xy,i}$ at fixed x_s increased as we moved away from the shock and as the
 735 mixture instability increased. A double peak can be observed in the regular case, whereas
 736 the dispersion became more uniform in the irregular case.

737 This subsection presents the comparison of the Favre average 1D profiles in terms of
 738 Eulerian and Lagrangian point of view on the mean structure for the gaseous detonation.

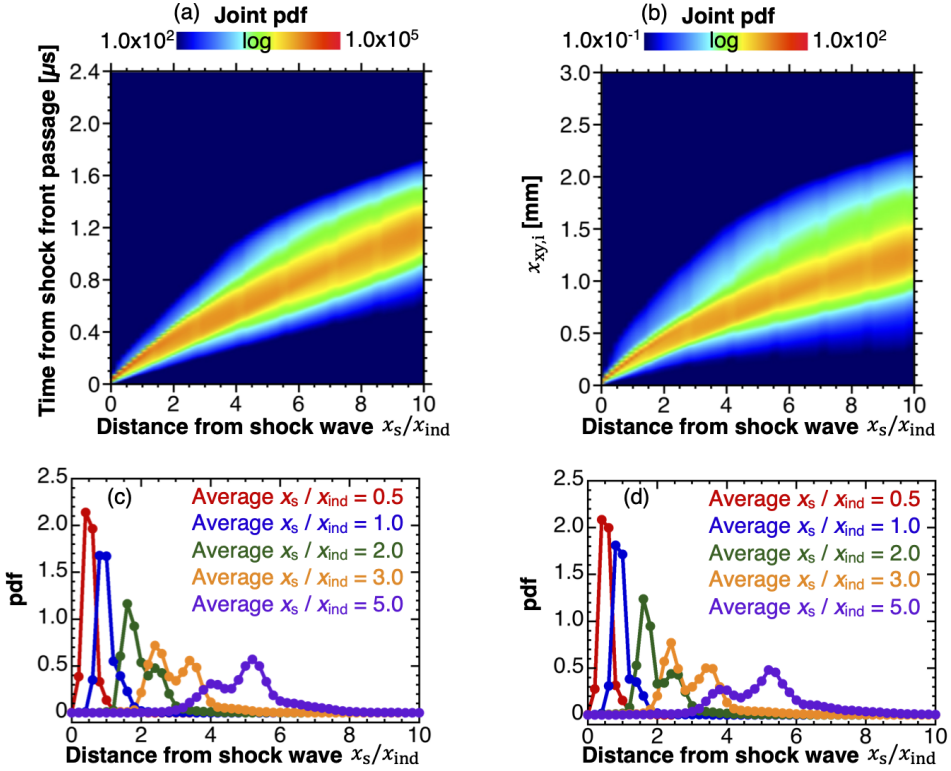


Figure 25: Distribution of τ and $x_{xy,i}$ as a function of the longitudinal distance from shock front in $2 \text{ H}_2 - \text{O}_2 - 7 \text{ Ar}$ mixture. (a) Joint pdf between the longitudinal distance from shock front x_s and time from shock front passage τ , (b) Joint pdf between x_s and the distance traveled by the particle along the trajectory $x_{xy,i}$, (c) pdf of x_s at several $x_{xy,i}$.

739 The Reynolds average values in the Eulerian mean procedure $\overline{G}_{\text{EUL}}$ for the variable G are
 740 computed by Eq. 4.10 (Watanabe et al. 2020):

$$741 \quad \overline{G}_{\text{EUL}}(x_s) = \frac{1}{H} \int_0^H \lim_{T_s \rightarrow \infty} \left(\frac{1}{T_s} \int_0^{T_s} G(x - x_{\text{shock}}(y, t), y, t) dt \right) dy \quad (4.10)$$

743 Here, $x_{\text{shock}}(y, t)$ is the instantaneous x position of the leading shock front, which is
 744 not straight due to cellular instabilities, H is the channel width, and T_s is the period of
 745 sampling, respectively. The longitudinal distance from the leading shock front $x_s = x - x_{\text{shock}}$
 746 perpendicular to the propagation direction is used for the Eulerian averaging process. The
 747 time from the shock passage τ and the distance x_{xy} traveled by Lagrangian particle from
 748 shock passage can thus be also candidates for the Lagrangian averaging procedures. Two
 749 Lagrangian average procedures have been proposed. The first consisted in computing the
 750 Reynolds average values in the Lagrangian mean procedure based on the time from shock
 751 passage $\overline{G}_{\text{LAG,time}}$, as in Eq. 4.11. The second one consisted in computing the Reynolds average
 752 values in the Lagrangian average procedure based on the distance traveled by Lagrangian

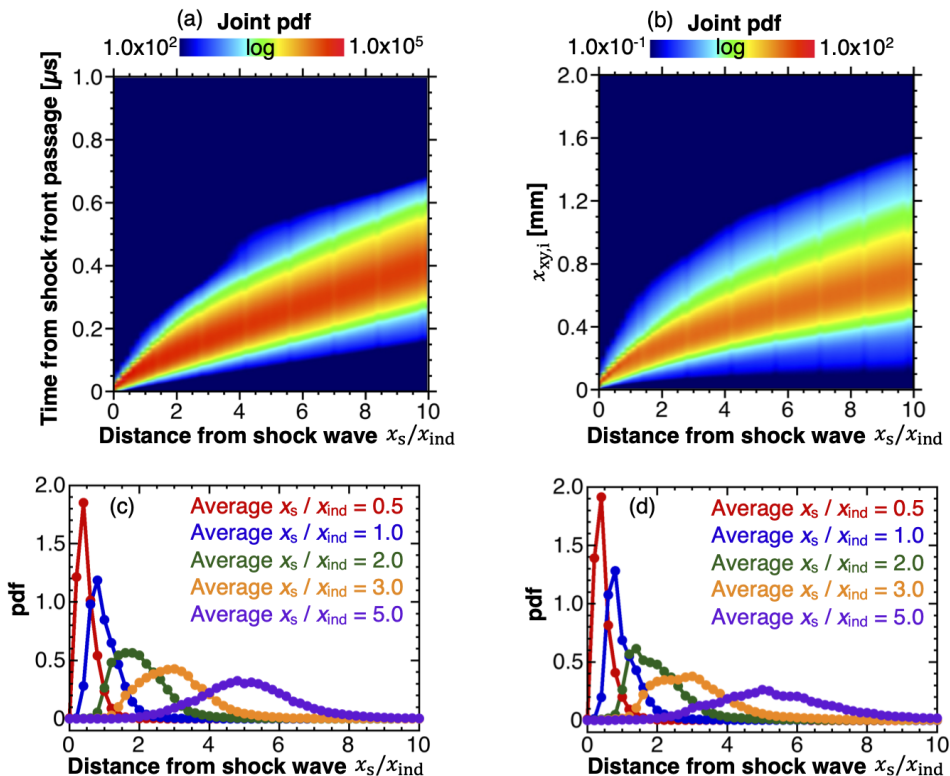


Figure 26: Distribution of τ and $x_{xy,i}$ as a function of the longitudinal distance from shock front in $2 \text{H}_2 - \text{O}_2$ mixture. (a) Joint pdf between the longitudinal distance from shock front x_s and time from shock front passage τ , (b) Joint pdf between x_s and the distance $x_{xy,i}$, (c) pdf of x_s at several τ , (d) pdf of x_s at several $x_{xy,i}$.

753 particle $\bar{G}_{\text{LAG,dist}}$, as in Eq. 4.12.

$$754 \quad \bar{G}_{\text{LAG,time}}(\tau) = \frac{1}{N} \sum_{i=1}^N G_i(\tau) \quad (4.11)$$

$$755 \quad \bar{G}_{\text{LAG,dist}}(x_{xy}) = \frac{1}{N} \sum_{i=1}^N G_i(x_{xy}) \quad (4.12)$$

756

757 where G_i is the value of the parameter at hand on particle i , $\tau = t - t_{\text{shock}}$ is the time elapsed
 758 from shock passage, x_{xy} is the post-shock distance traveled by the particle, and N is the
 759 number of particles sampled.

760 Then, from the different Reynolds averaging procedures, the Favre average quantities
 761 can be obtained from Reynolds averaged conservative variables $\bar{\eta} = \overline{\rho\eta}/\bar{\rho}$, where η is the
 762 conservative variable (Favre 1965).

763 In order to enable the comparison between \bar{G}_{EUL} and $\bar{G}_{\text{LAG,time}}$, we need to map the time
 764 elapsed from shock passage up to the longitudinal distance from the shock location $x_{s,\text{time}}$.
 765 The following mapping will be used in Eq. 4.11:

$$766 \quad x_{s,\text{time}} = \int_0^\tau (\bar{D} - \tilde{u}) d\tau \quad (4.13)$$

767

Mixtures	τ_c (μs) - Figures	Correlation coefficients
$2\text{H}_2\text{-O}_2\text{-7Ar}$	5 - Fig. 30(a)	$\sigma_{x'_i(t_0)x'_i(t_0+\tau_c)}$ 0.98
	20 - Fig. 30(b)	$\sigma_{x'_i(t_0)x'_i(t_0+\tau_c)}$ 0.89
	5 - Fig. 30(c)	$\sigma_{y'_i(t_0)y'_i(t_0+\tau_c)}$ 0.98
	20 - Fig. 30(d)	$\sigma_{y'_i(t_0)y'_i(t_0+\tau_c)}$ 0.90
$2\text{H}_2\text{-O}_2$	2 - Fig. 31(a)	$\sigma_{x'_i(t_0)x'_i(t_0+\tau_c)}$ 0.84
	8 - Fig. 31(b)	$\sigma_{x'_i(t_0)x'_i(t_0+\tau_c)}$ 0.70
	2 - Fig. 31(c)	$\sigma_{y'_i(t_0)y'_i(t_0+\tau_c)}$ 0.88
	8 - Fig. 31(d)	$\sigma_{y'_i(t_0)y'_i(t_0+\tau_c)}$ 0.81

Table 3: Correlation coefficients between displacements at t_0 and at $t_0 + \tau_c$.

Mixture	Characteristic lengths	Averaging procedure		
		Eulerian	Lagrangian (distance)	Lagrangian (time)
$2\text{H}_2\text{-O}_2\text{-7Ar}$	Induction length	1.1	1.1	1.0
	Reaction length	3.8	3.9	3.9
	Hydrodynamic thickness	115.0	117.7	117.0
	Average cell width	17.0	-	-
$2\text{H}_2\text{-O}_2$	Induction length	0.9	1.0	0.8
	Reaction length	0.8	0.8	0.8
	Hydrodynamic thickness	129.6	149.6	134.6
	Average cell width	14.4	-	-

Table 4: Characteristic lengths normalized by induction length for $2\text{H}_2\text{-O}_2\text{-7Ar}$ and $2\text{H}_2\text{-O}_2$ mixtures. Nondimensionalized cell widths are added for comparison. The Lagrangian (distance) stands for the averaging process, described by Eqs. 4.12,4.14 and Lagrangian (time) refers to procedure based on Eqs. 4.11,4.13.

768 Here, \bar{D} is the average propagation velocity of the detonation front and is equal to D_{CJ} in the
769 present simulation conditions. In order to map the distance traveled by Lagrangian particle
770 from the shock passage to the longitudinal distance from the shock location based on the
771 distance traveled by the Lagrangian particle $x_{\text{s,dist}}$, the following mapping will be used in
772 Eq. 4.12 for $\bar{G}_{\text{LAG,dist}}$:

$$773 \quad x_{\text{s,dist}} = \int_0^\tau (\bar{D} - \tilde{u}) dt \text{ such as } dt = dx_{\text{xy}} / [\tilde{u}^2 + \tilde{v}^2]^{1/2} \quad (4.14)$$

775 Here, \tilde{u} and \tilde{v} are the Lagrangian Favre averages of the x and y components of the velocity
776 in the laboratory frame. Figure 27 depicts the relations (Eqs. 4.13 and 4.14) between the
777 distance from the shock front, the time from shock passage and the longitudinal distance from
778 shock location. The results of the two Lagrangian procedures and the ZND model agreed
779 well with each other, meaning that the procedures to convert the target values used in the
780 Lagrangian procedures into the longitudinal distance from the shock front are appropriate.

781 The effects of the distance traveled by the particle and the time elapsed from the shock
782 passage are not taken into account into the Eulerian procedure. However, the time elapsed
783 from the shock passage is more relevant as far as chemical reactions are concerned. There
784 are also differences between the two Lagrangian procedures. Indeed, the difference is more

785 apparent especially in the boundary layer. Due to the lower velocity in the boundary layer,
 786 the distance x_{xy} does not increase as that in the core of the flow, for the same time elapsed
 787 from shock passage.

788 The comparison of the Favre average 1D profiles in the instantaneous shock frame for
 789 $2\text{H}_2\text{-O}_2\text{-7Ar}$ and $2\text{H}_2\text{-O}_2$ mixtures are depicted in Figs. 28 and 29, respectively. The frozen
 790 sound speed was used to estimate the Mach number in Figs. 28(d) and 29(d). The trends for
 791 the profiles of pressure, temperature and Mach number were nevertheless similar regardless
 792 of the Favre average procedure, either from the Eulerian or the Lagrangian point of view.
 793 Slight oscillations in Lagrangian Favre averages are observed near the front for the diluted
 794 case. In all cases, the profiles differed from that of the ZND solution. Indeed, Radulescu et
 795 al. (2007) and Sow et al. (2014) showed that the fluctuations delayed the energy deposition.
 796 Lalchandani (2022) developed a physical model that explained the slower rate of the heat
 797 release by the decaying of the shock velocity inside the cell.

798 As for the regular case (Fig. 28), the distributions of the chemical species, the thermicity
 799 and the other variables in Lagrangian and Eulerian results were almost identical. On the
 800 other hand, as for the irregular case, the width of the thermicity was wider (Figs. 28(c,e,f,g)
 801 and 29(c,e,f,g)). The increasing part of the curves was similar, whereas differences were
 802 apparent in the decreasing part of the thermicity, after its peak. All the other profiles then
 803 followed the same trend: Eulerian results matched the Lagrangian results before the peak of
 804 thermicity, with Lagrangian results decreasing more smoothly afterwards. Less differences
 805 were observed in the pressure and Mach number profiles. The maximum differences for the
 806 H_2 mass fraction were located after the peak of thermicity. They reached 12% and 18%
 807 between the Eulerian and Lagrangian time and distance averages for the diluted mixture and
 808 increased up to 33% and 36% for the other mixture.

809 Based on the reduced activation energy and the related stability analysis for the emergence
 810 of longitudinal disturbances in 1D cases, the mixtures could be classified as weakly and mildly
 811 unstable. Transverse disturbances then came into play in 2D configurations. As argued at first
 812 by Radulescu et al. (2007) and by many others (Maxwell et al. 2017; Taileb et al. 2018;
 813 Reynaud et al. 2020; Sow et al. 2021), the fluctuations and the induced dispersion explain
 814 the differences between the mean quantities from numerical simulations and the ZND results.
 815 All dispersion quantities ($\overline{x_i'^2}$, $\overline{y_i'^2}$), when nondimensionalized by $E_a/(RT_{vN}) \cdot x_{\text{ind}}$ were found
 816 to be self-similar in the time τ/τ_{ind} . This good agreement suggests that the dispersion could
 817 result from an one-dimensional instability mechanism only. It may thus originate from the
 818 fluctuations of the leading shocks that induce the induction and reaction length fluctuations,
 819 with transverse waves being a necessary corollary.

820 On the other hand, the relative dispersion was also found to be self-similar in the time
 821 τ/τ_{ind} , after the main heat release zone, when the relative dispersion was normalized by
 822 $\chi \cdot x_{\text{ind}}$, with χ considered as a dimensionless acceleration. Both mixtures lie on either side
 823 on the neutral stability curve. Small values of χ imply that the pulses of heat release of
 824 neighbouring particles will overlap (Radulescu 2003). On the other hand, if this χ parameter
 825 is larger, gasdynamic instabilities result from the lack of coherence of the power pulses and
 826 discreteness, and led to the deviations observed in the Eulerian and Lagrangian averaging
 827 processes after the peak thermicity for the irregular case.

828 The value of the specific heat ratio at vN state for non diluted case is 1.32 and was
 829 very close to the boundary where Mach bifurcation occurs due to jetting after triple point
 830 collision (Lau-Chapdelaine et al. 2021; Sow et al. 2021), which results in more mixing
 831 behind the front. For the range of γ_{vN} investigated in this study, the impact of compressibility
 832 (see Fig. 7 in Sow et al. (2021)) can be estimated to be low.

833 Figures 30 and 31 show the joint pdf of the fluctuations of the displacements $x'_i = (x_{p,i} -$

Lagrangian Favre average based on distance traveled from shock passage (2H₂-O₂-7Ar)
 Lagrangian Favre average based on time from shock passage (2H₂-O₂-7Ar)
 ZND (2H₂-O₂-7Ar)
 Lagrangian Favre average based on distance traveled from shock passage (2H₂-O₂)
 Lagrangian Favre average based on time from shock passage (2H₂-O₂)
 ZND (2H₂-O₂)

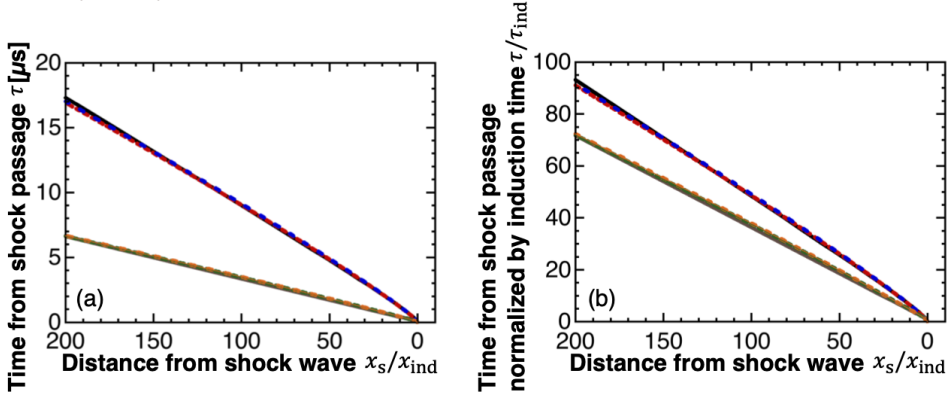


Figure 27: Lagrangian Favre average 1D profiles for both mixtures (a) x_s / x_{ind} and τ , (b) x_s / x_{ind} and τ / τ_{ind} .

834 $x_{p,i,0} - \overline{(x_{p,i} - x_{p,i,0})}$ and $y'_i = (y_{p,i} - y_{p,i,0})$ at a certain instant t_0 with that at a later
 835 time $t_0 + \tau_c$, τ_c being equal to approximately $\sim \tau_{HT}/2$ and $\sim 2\tau_{HT}$, where τ_{HT} is the time
 836 corresponding to the hydrodynamic thickness. If the motion were to be brownian, the shape
 837 of the joint pdf would correspond to a circle. Instead, in both cases, the joint pdf lied along
 838 positive lines, meaning that they are positively correlated to each other. One can see that the
 839 shape of the joint pdf got rounder as time passed, all the more so as we got outside the mean
 840 detonation driving zone (DDZ). Table 3 lists the correlation coefficients for the joint pdf of
 841 Figs. 30 and 31 that were very high.

842 Table 4 lists the characteristic lengths for both mixtures for the different Favre averaging
 843 procedures. The induction and reaction lengths were almost the same. The position of the
 844 peak thermicity can be captured regardless of the average method. Only a slight variation
 845 was observed for the hydrodynamic thickness for the irregular case after the peak thermicity.
 846 Therefore, the Eulerian Favre average procedure gave the mean structure of the gaseous
 847 detonation with a reasonable accuracy.

848 5. Conclusions

849 Two-dimensional simulations with the Lagrangian particle tracking method were conducted
 850 for a weakly and a mildly unstable hydrogen-based mixtures at ambient conditions. Two
 851 new Lagrangian Favre average procedures, based on the distance traveled by the particle
 852 or the time from the shock passage were proposed and 1D profiles were compared with
 853 those from Eulerian procedure, based on the longitudinal distance from the shock front.
 854 The integral length was the hydrodynamic thickness that encompasses the mean detonation
 855 driving zone from the leading shock to the mean sonic line. The results from the Eulerian
 856 and Lagrangian averaging processes gave similar induction length, reaction length and
 857 hydrodynamic thickness. The Eulerian results gave the mean structure with a reasonable
 858 accuracy. As the mixture instability increased, the Lagrangian results were smoother after
 859 the thermicity peak than the Eulerian results.

860 Dispersion is inherent to the detonation driving zone, due to the fluctuations of the leading

ZND

Eulerian Favre average

Lagrangian Favre average based on distance traveled from shock passage

Lagrangian Favre average based on time from shock passage

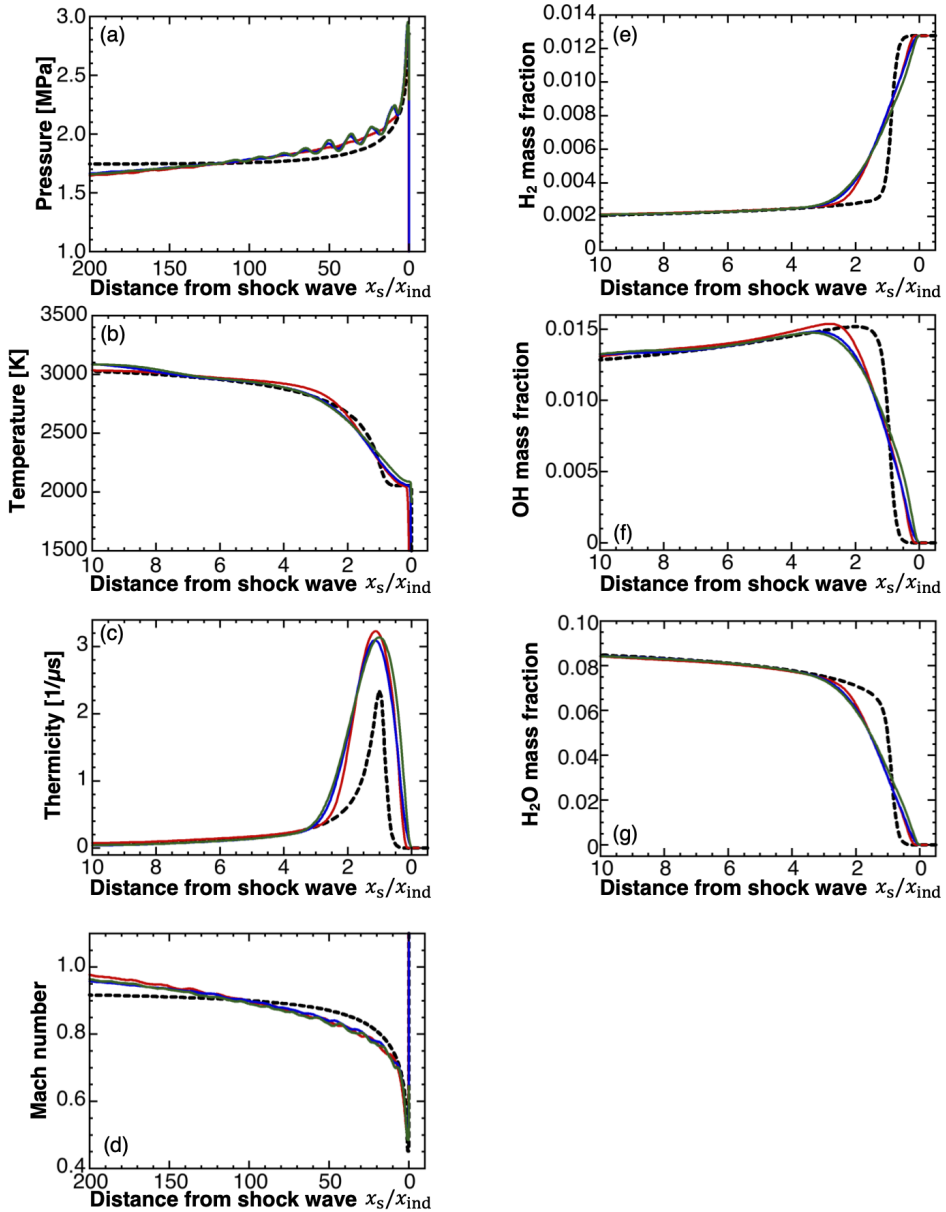


Figure 28: Favre average 1D profiles in $2\text{H}_2\text{-O}_2\text{-7Ar}$ mixture for (a) pressure, (b) temperature, (c) thermicity, (d) Mach number, (e) H_2 mass fraction, (f) OH mass fraction, and (g) H_2O mass fraction.

861 shock and its curvature, the presence of the reaction front, transverse waves, forward and
 862 backward jets, vortical structures, and boundary layer. The latter was minor as the detonation
 863 was ideal with no losses. The main findings were that dispersion could be scaled with
 864 $E_a/(RT_{\text{VN}}) \cdot x_{\text{ind}}$ and that the relative dispersion far from the shock, scaled by $\chi \cdot x_{\text{ind}}$ with

ZND

Eulerian Favre average

Lagrangian Favre average based on distance traveled from shock passage

Lagrangian Favre average based on time from shock passage

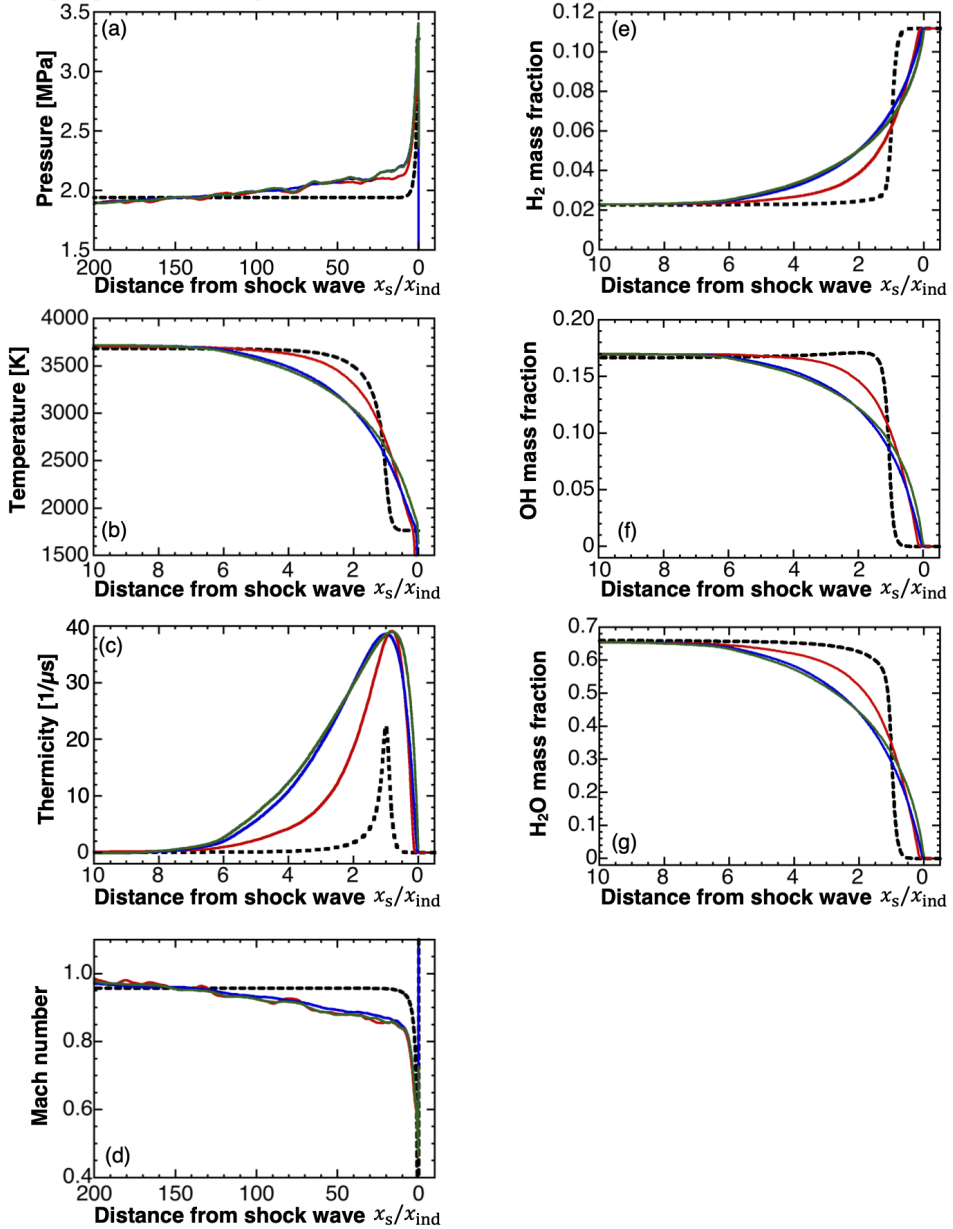


Figure 29: Favre average 1D profiles in $2\text{H}_2\text{-O}_2$ mixture for (a) pressure, (b) temperature, (c) thermicity, (d) Mach number, (e) H_2 mass fraction, (f) OH mass fraction, and (g) H_2O mass fraction.

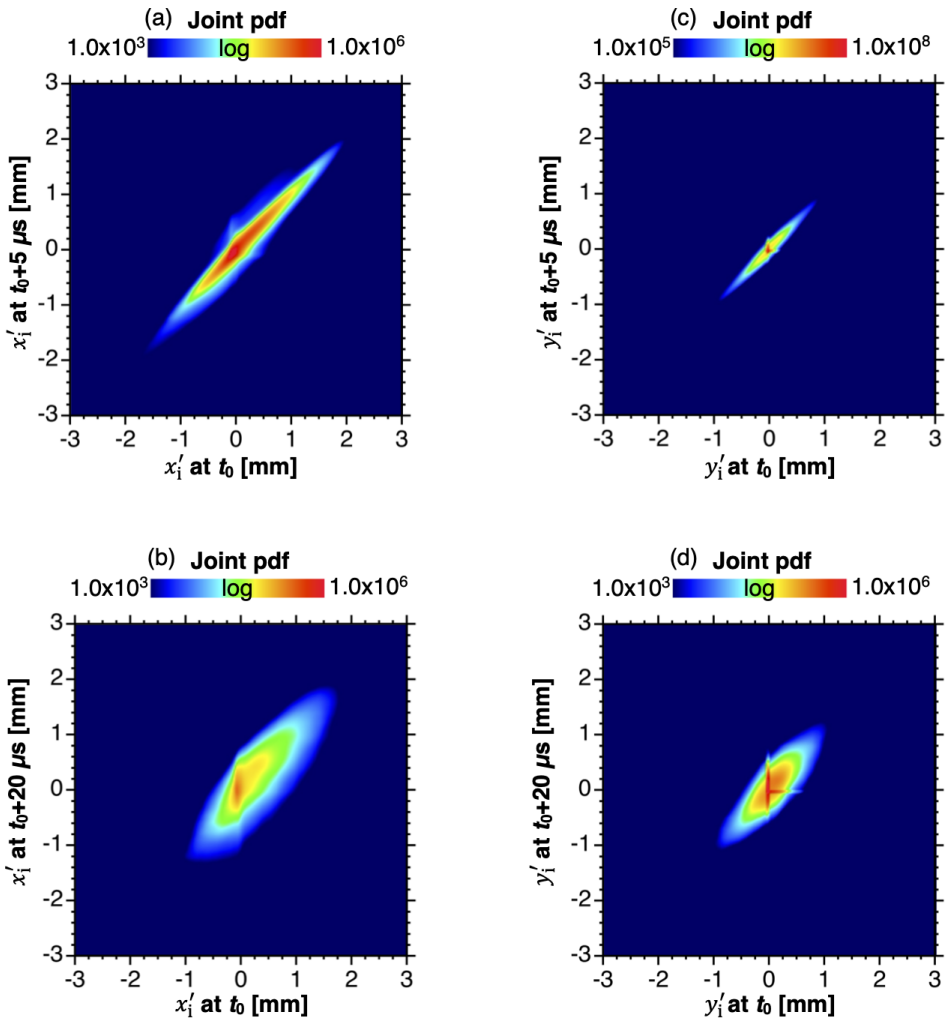


Figure 30: Joint pdf between displacement fluctuations at t_0 and that at $t_0 + \tau_c$ in $2\text{H}_2 - \text{O}_2 - 7\text{Ar}$ mixture. (a) x'_1 displacement fluctuations with $\tau_c = 5\ \mu\text{s}$, (b) x'_1 displacement fluctuations with $\tau_c = 20\ \mu\text{s}$, (c) y'_1 displacement fluctuations with $\tau_c = 5\ \mu\text{s}$, (d) y'_1 displacement fluctuations with $\tau_c = 20\ \mu\text{s}$.

865 χ as a dimensionless acceleration. The fact that these instability parameters were successful
 866 for these scalings strongly suggests that the main mechanism driving the dispersion was the
 867 one-dimensional leading shock fluctuations, i.e. its decaying and amplification upon triple
 868 shock collision within the cell. For more highly unstable mixtures with larger $E_a/(RT_{vN})$
 869 and χ , the presence of more frequent unburnt pockets of fresh gases along with their burning
 870 mechanisms can circumscribe these findings. Moreover, the displacement fluctuations at
 871 a given time was positively correlated to the displacement fluctuations at a later time,
 872 corresponding to about the hydrodynamic thickness time scale.

873 The dispersion in the induction time scale was closely related to the cellular structure.
 874 Particles are not only accumulated between the locations of the transverse wave and triple
 875 point collisions but were also along the triple point trajectories. Another finding was that as
 876 the mixture instability increased, the contribution of the transverse waves along the triple

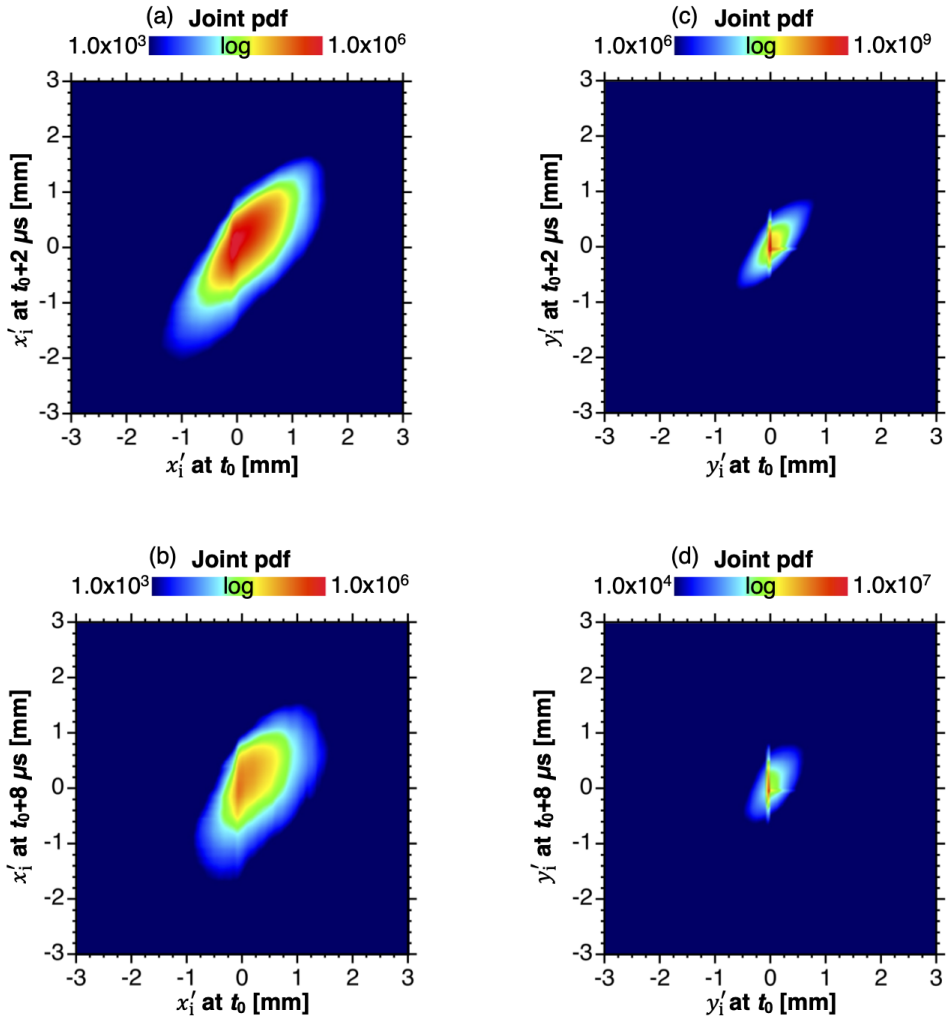


Figure 31: Joint pdf between displacement fluctuations at t_0 and that at $t_0 + \tau_c$ in $2\text{H}_2 - \text{O}_2$ mixture. (a) x'_i displacement fluctuations with $\tau_c = 2\ \mu\text{s}$, (b) x'_i displacement fluctuations with $\tau_c = 8\ \mu\text{s}$, (c) y'_i displacement fluctuations with $\tau_c = 2\ \mu\text{s}$, (d) y'_i displacement fluctuations with $\tau_c = 8\ \mu\text{s}$.

877 point trajectories in the accumulation of the particles increased. The differences with the
 878 physical picture of cell size model relying on discrete blast dynamics were more apparent.
 879 The induction process was completed within first half of the cell cycle in the diluted case,
 880 whereas more variation in the induction time could be found in the non diluted case due to
 881 the higher activation energy and the presence of unburnt pockets. Within the induction time
 882 scale, the transverse dispersion was mainly due to the curvature of the leading shock. This
 883 effect was more pronounced near the edges of the cell and during the first part of the cell,
 884 when the leading detonation front was a Mach stem.

885 The detonation could be described as a two-scale phenomenon, specially for the unstable
 886 mixture. The first scale, of a few induction lengths about $5 \sim 10 x_{\text{ind}}$, could be related to
 887 the main heat release zone, from the shock up to the vicinity of the peak thermicity. The
 888 influence of the transverse waves was still present. Indeed, the levels of y'_i were about those

889 of x'_1 . Then after a transient, a new zone was present. The transverse y'_1 decreased, leading
 890 to small anisotropic dispersion ($[\overline{y'_1{}^2/x'_1{}^2}]^{1/2} \sim 0.6$). The Richardson-Obukhov scaling law
 891 surprisingly still holded, in the zone of small heat release after the peak thermicity, suggesting
 892 that classical non reacting laws of turbulence may remain relevant. Only the unstable case
 893 approached the R-O scaling within the mean detonation driving zone.

894 The dispersion of the Lagrangian particles was promoted behind the detonation front.
 895 We could try to sort out the production of these fluctuations: x displacements due to the
 896 decaying detonation front (one dimensional instability mechanism), then y displacements
 897 due to the curvature of the leading inert shock front and the presence of the reaction front
 898 (due to density ratio). The variation of the distance between the leading shock and the
 899 reaction front in the transverse direction induced further transverse dispersion (maximum
 900 of $\overline{y'_1{}^2/x'_1{}^2}$ around $2\tau_{\text{ind}}$). Even if the reactive transverse waves were present in the diluted
 901 case, and some unburnt pockets in the non diluted case, these differences do not manifest
 902 themselves on the dispersion of the Lagrangian particles (collapse of the histories of scaled
 903 $\overline{x'_1{}^2/(E_a/(RT_{\text{vN}} \cdot x_{\text{ind}}))^2}$ and $\overline{y'_1{}^2/x'_1{}^2}$). In our case, due to high isentropic coefficients, the jets
 904 have not induced any cell bifurcation.

905 The study of the derivative of the relative dispersion with respect with time showed that
 906 after the main heat release, the relative dispersion relaxed towards the Richardson-Obukhov
 907 regime (exponent near 3), specially for the non diluted case. The influence of the vortical
 908 motions coming from the jets and the slip lines, the fading of the transverse waves can not
 909 be ignored in this transition.

910 Moreover, the exponent of the pdf for the relative dispersion was also consistent with
 911 Richardson's prediction in unstable case. Furthermore, the pdf for the relative dispersion
 912 was self-similar in time. Nevertheless, the velocity field was not short time correlated with a
 913 separation distance below the induction length, meaning that the dispersion process could not
 914 be described by the diffusive equation. The relative dispersion scaled with the χ parameter,
 915 which suggested that the rapid energy deposition on the reaction length scale also contributed
 916 to this phenomenon.

917 In addition, the present finding on the velocity field behind the detonation front can help
 918 to develop a turbulent model for detonation. Lagrangian averaging can have a merit over that
 919 from Eulerian results despite its higher computational cost. Conditional pdf as in dispersed
 920 detonation flows (Watanabe et al. 2021) could improve our understanding of the links
 921 between pressure, vortical, entropy modes and chemistry in detonation.

922 **Acknowledgements.** AC and HW would like to thank Vincent Robin from Institut Pprime for many fruitful
 923 discussions and many advice. HW and AC are very grateful for the comments and suggestions by the
 924 anonymous referees during the revision of the manuscript.

925 **Funding.** This research was subsidized by JSPS KAKENHI Grant number JP20K22391(Grant-in-Aid for
 926 Research Activity Start-up), JP21K14094(Grant-in-Aid for Early-Career Scientists), JP19J12758(Grant-in-
 927 Aid for Specially Promoted Research), the Paloma Environmental Technology Development Foundation, and
 928 the CPER FEDER Project of Région Nouvelle Aquitaine and pertains to the French government program
 929 "Investissements d'Avenir" (EUR INTREE, reference ANR-18-EURE-0010). HW is supported by JSPS
 930 Overseas Research Fellowships.

931 **Declaration of interests.** No potential conflict of interest was reported by the authors.

932 Appendix A. Assessment of numerical convergence

933 In this appendix, the numerical convergence was assessed to check the effect of the
 934 grid resolution on the simulation results. The high computational cost for the numerical
 935 simulations with the Lagrangian particle tracking method prevented us to use higher grid

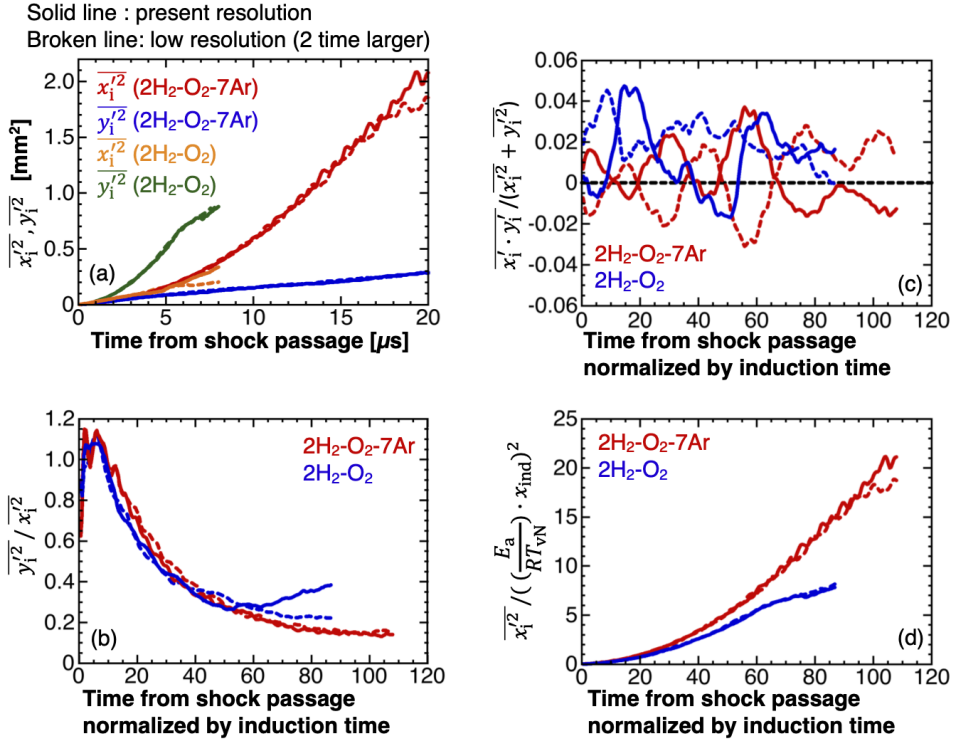


Figure 32: Average dispersion in 2H₂-O₂-7Ar and 2H₂-O₂ mixtures with two different grid resolutions. (a) Time history of $\overline{x_i'^2}$ and $\overline{y_i'^2}$, (b) $\overline{y_i'^2}/\overline{x_i'^2}$ as a function of τ/τ_{ind} , (c) $\overline{x_i' \cdot y_i'} / (\overline{x_i'^2} + \overline{y_i'^2})$, (d) $\overline{x_i'^2} / ((E_a / (RT_{vN})) \cdot x_{ind})^2$ as a function of τ/τ_{ind} .

936 resolution than that used in the present study. According to previous studies, the present grid
 937 resolution satisfied the requirement for the grid resolution for the convergence of the 1D
 938 average profiles (Reynaud et al. 2017, 2020) for both mixtures and a reasonable physical
 939 structure in the instantaneous 2D flow field (Mazaheri et al. 2012) in 2H₂-O₂-7Ar mixture.

940 The numerical convergence was assessed by comparing the simulation results using coarser
 941 grid, which was two times larger than the one used for the main results. The same simulation
 942 conditions were used and the propagation velocity was the same regardless of the grid
 943 resolution. In addition, the average cell width in the simulation from the manual measurement
 944 of 150 and 300 cells for 2H₂-O₂-7Ar and 2H₂-O₂ mixture in the coarse grid was 1.3 mm
 945 and 0.7 mm, respectively. The average cell width agreed well between the two different grid
 946 resolutions.

947 The comparison of the average dispersion between the two different grid resolutions
 948 was shown in Fig. 32. Although minor differences were observed, the profiles for average
 949 dispersion with different grid resolutions were similar (Fig. 32).

950 The effect of the grid resolution on the relative dispersion was also evaluated. The
 951 initial distance between two particles in the same pair was doubled, as compared to the
 952 computations shown in Section 4.3. Figure 33 depicts the average relative dispersion for 2H₂-
 953 O₂-7Ar and 2H₂-O₂ mixtures. The profiles were similar between the two grid resolutions.
 954 In 2H₂-O₂ mixture, the differences could be seen, as the time from shock passage increased.
 955 Nevertheless, the average relative dispersion \overline{r}_{xy} normalized by the characteristic length scale

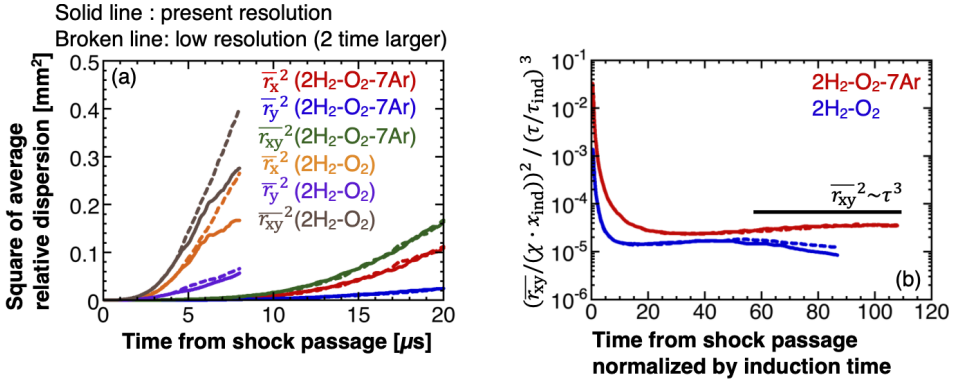


Figure 33: Average relative dispersion in $2\text{H}_2\text{-O}_2\text{-7Ar}$ and $2\text{H}_2\text{-O}_2$ mixtures with two different grid resolutions. (a) Average relative dispersion $\overline{r_x}^2$, $\overline{r_y}^2$, $\overline{r_{xy}}^2$, as a function of time passage τ , (b) time history of normalized $(\overline{r_{xy}}/(\chi \cdot x_{\text{ind}}))^2$ compensated by normalized $(\tau/\tau_{\text{ind}})^3$.

956 $\chi \cdot x_{\text{ind}}$ as a function of the time from shock front passage τ/τ_{ind} showed similar trends for
 957 both grid resolutions, meaning that the scaling worked well and that the R-O law still held.

958 The comparisons of the Favre average 1D profiles in the instantaneous shock frame from
 959 Eulerian and Lagrangian point of view using the two different grid resolutions for $2\text{H}_2\text{-}$
 960 $\text{O}_2\text{-7Ar}$ and $2\text{H}_2\text{-O}_2$ mixtures are depicted in Figs. 34 and 35. The characteristic lengths
 961 estimated from the Favre average 1D profiles in the coarse grid are listed in Table 5.

962 In $2\text{H}_2\text{-O}_2\text{-7Ar}$ mixture, the Favre average 1D profiles for pressure, H_2 mass fraction,
 963 Mach number and thermicity were well converged between the two different grid resolution
 964 regardless of the Favre average procedure (Fig. 34). The Favre average 1D profiles from
 965 Eulerian procedure for $2\text{H}_2\text{-O}_2$ mixture were also similar between the two different grid
 966 resolutions (Fig. 35), except some minor differences.

967 Therefore, the characteristic lengths were similar between the two different grid resolutions.
 968 Moreover, the mean structure was also well captured by the present grid resolution (Tables 4
 969 and 5). This observation on the effect of grid resolution on the mean structure was in line
 970 with the previous studies (Reynaud et al. 2017, 2020).

971 Thus, the profiles used for the analysis were well captured in the present grid resolution,
 972 and the conclusions on the Lagrangian dispersion and the mean structure in this study were
 973 not called into question by the numerical resolution.

974 Appendix B. Evaluation of anisotropy from the fluctuations in displacement

975 The dispersion was anisotropic (see Fig. 12(b)), where $[\overline{y_i'^2}/\overline{x_i'^2}]^{1/2}$ decreased from one near
 976 the front to two thirds at the end of the DDZ. To quantify further this dispersion, the joint pdf
 977 between x_i' and y_i' is depicted in Figs. 36 and 37 for different instants to show their evolution.
 978 The centers are determined where $x_i' = y_i' = 0$. The boundary of the joint pdf shape was
 979 taken at 10^4 . The roundness and relative roundness were then evaluated as a measurement of
 980 the anisotropy (see Eqs. B 1 and B 2).

$$981 \quad R_n = \max((e_{x,p} + e_{x,n}), (e_{y,p} + e_{y,n})) - \min((e_{x,p} + e_{x,n}), (e_{y,p} + e_{y,n})) \quad (\text{B } 1)$$

$$982 \quad R_{n,r} = R_n / \max((e_{x,p} + e_{x,n}), (e_{y,p} + e_{y,n})) \quad (\text{B } 2)$$

984 Here, $e_{x,p}$ and $e_{x,n}$ are the distances from the center to the edges of the boundary in the

Solid line : present resolution (2.0 μm)

Broken line: low resolution (4.0 μm)

ZND

Eulerian Favre average

Lagrangian Favre average based on distance along trajectory xy

Lagrangian Favre average based on time from shock front passage

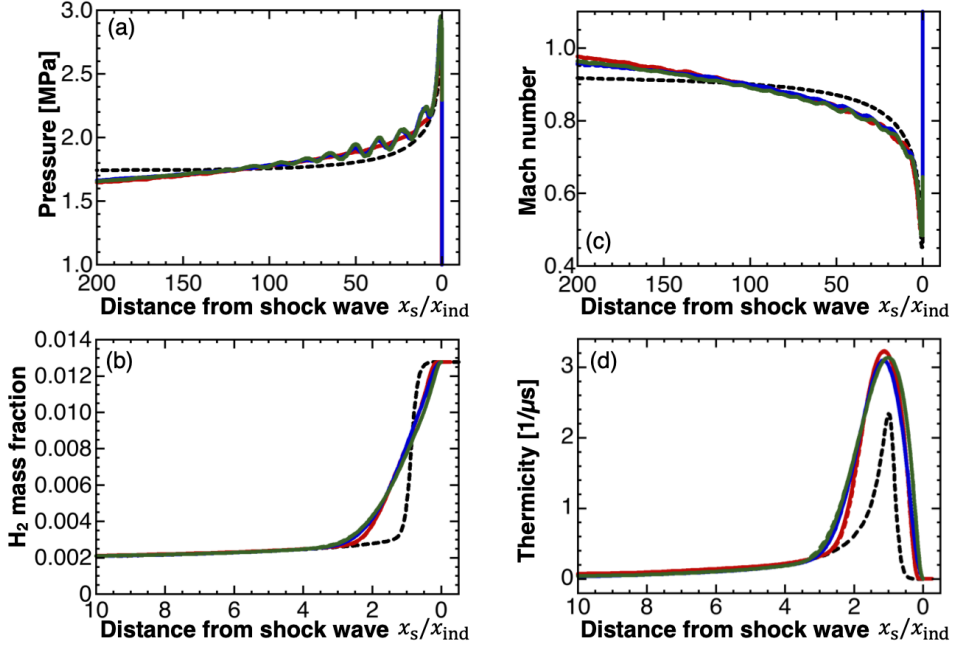


Figure 34: Favre average 1D profiles in $2\text{H}_2\text{-O}_2\text{-7Ar}$ mixture with two different grid resolutions for (a) pressure, (b) H_2 mass fraction, (c) Mach number, (d) thermicity.

Mixture	Characteristic lengths	Averaging procedure		
		Eulerian	Lagrangian (distance)	Lagrangian (time)
$2\text{H}_2\text{-O}_2\text{-7Ar}$	Induction length	1.1	1.1	1.0
	Reaction length	3.8	3.9	3.9
	Hydrodynamic thickness	114.4	117.9	116.2
	Average cell width	17.0	-	-
$2\text{H}_2\text{-O}_2$	Induction length	0.9	1.0	0.8
	Reaction length	0.8	0.8	0.8
	Hydrodynamic thickness	129.2	154.8	154.4
	Average cell width	14.2	-	-

Table 5: Characteristic lengths normalized by induction length for $2\text{H}_2\text{-O}_2\text{-7Ar}$ and $2\text{H}_2\text{-O}_2$ mixtures in the coarse grid resolution. Nondimensionalized cell widths are added for comparison. The Lagrangian (distance) stands for the averaging process, described by Eqs. 4.12,4.14 and Lagrangian (time) refers to procedure based on Eqs. 4.11,4.13.

Solid line : present resolution (1.6 μm)

Broken line: low resolution (3.2 μm)

ZND

Eulerian Favre average

Lagrangian Favre average based on distance along trajectory xy

Lagrangian Favre average based on time from shock front passage

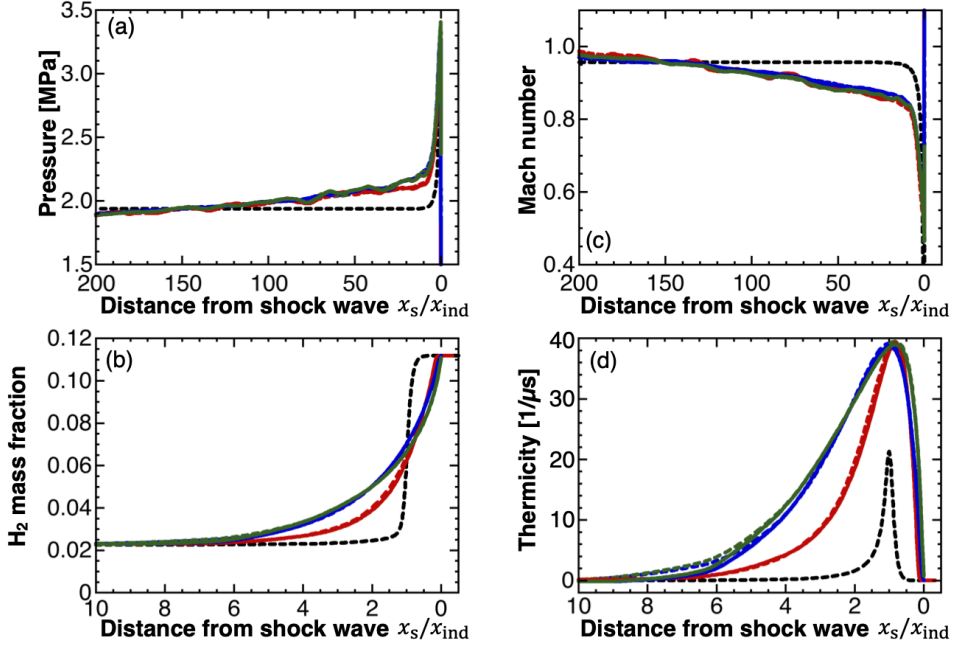


Figure 35: Favre average 1D profiles in 2H₂-O₂ mixture with two different grid resolutions for (a) pressure, (b) H₂ mass fraction, (c) Mach number, (d) thermicity.

985 x -axis, and in the same way for $e_{y,p}$ and $e_{y,m}$ in the y -axis. The roundness and relative
 986 roundness denote the degree of the symmetry of the joint pdf and its relative magnitude,
 987 respectively. Their values are listed in Table 6. The roundness was not zero and increased as
 988 time passed for both mixtures, which means that dispersion became anisotropic. However,
 989 the relative roundness rapidly saturated to 35% and to 40% for both mixtures, values of
 990 which are consistent with the ratio of $1 - [y_i'^2/x_i'^2]^{1/2} \sim 1/3$ found previously.

991 Appendix C. Pdfs of the relative dispersion, correlation coefficients and 992 characteristic time scales

993 The curves for the diffusive limit and the inertia regime are recalled here as they were included
 994 in Figs. 22(c-f) for comparison. The pdf for the relative dispersion in the diffusive limit f_{diff}
 995 is given by Eq. C1 (Buaria et al. 2015).

$$996 \quad \text{pdf}_{\text{diff}} = 3\sqrt{6/\pi}(r_{xy}/\overline{r_{xy}})^2 \exp\left[-\frac{3}{2}(r_{xy}/\overline{r_{xy}})^2\right] \quad (C1)$$

998 Richardson predicted the pdf for the relative dispersion in the inertia regime $\text{pdf}_{\text{inertia}}$ as
 999 follows (Sawford et al. 2013).

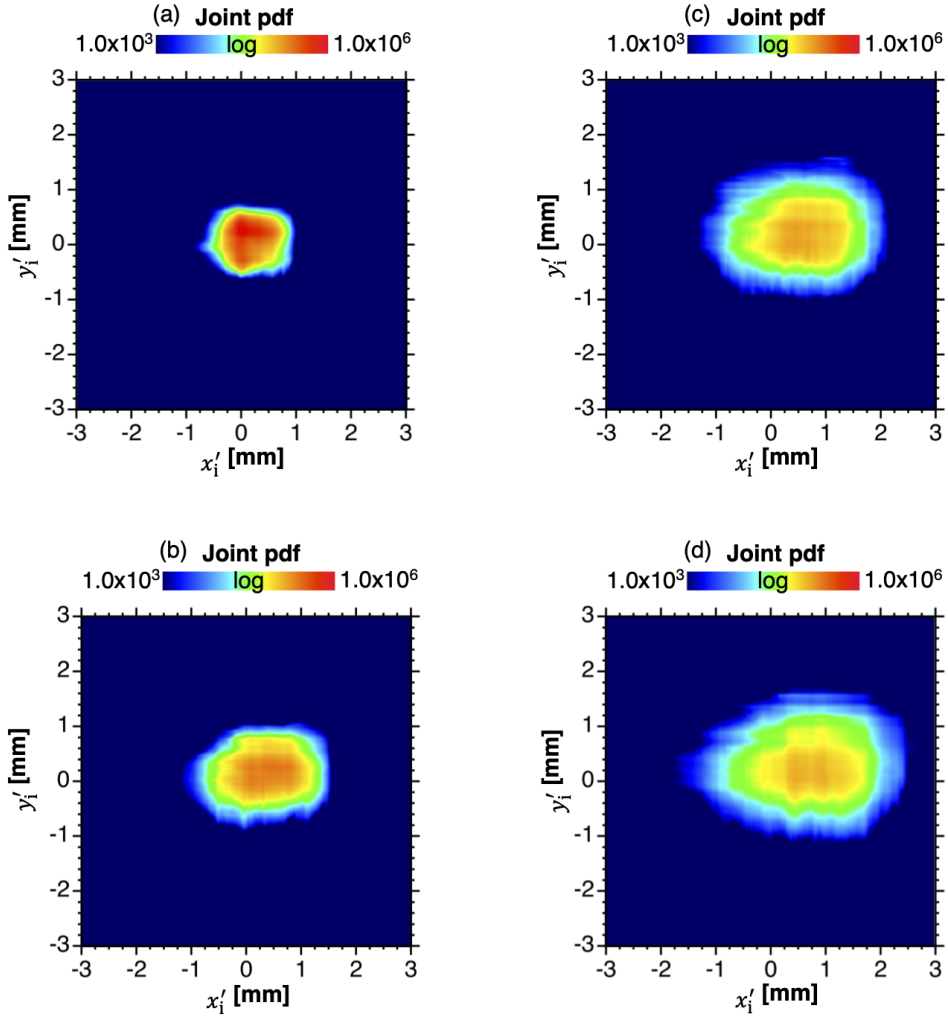


Figure 36: Joint pdf for $2\text{H}_2\text{-O}_2\text{-7 Ar}$ between the fluctuations of longitudinal displacements x'_1 and that of the transverse displacements y'_1 for different times from shock passage: (a) $5\ \mu\text{s}$, (b) $10\ \mu\text{s}$, (c) $15\ \mu\text{s}$, (d) $20\ \mu\text{s}$.

$$\text{pdf}_{\text{inertia}} = \left(\frac{1144}{81}\right)^{3/2} \left(\frac{2187}{560\sqrt{\pi}}\right) (r_{xy}/\overline{r_{xy}})^2 \exp\left[-\frac{9}{4} \left(\frac{1144}{81}\right)^{1/3} (r_{xy}/\overline{r_{xy}})^{2/3}\right] \quad (\text{C2})$$

1002 The characteristic times normalized by the induction time for both mixtures for the different
1003 Favre averaging procedure are listed in Table 7.

1004 The correlation coefficients between the displacements at t_0 and at $t_0+\tau_c$ in longitudinal and
1005 transverse directions in Table 3 are estimated by the following Eqs. C3 and C4, respectively.

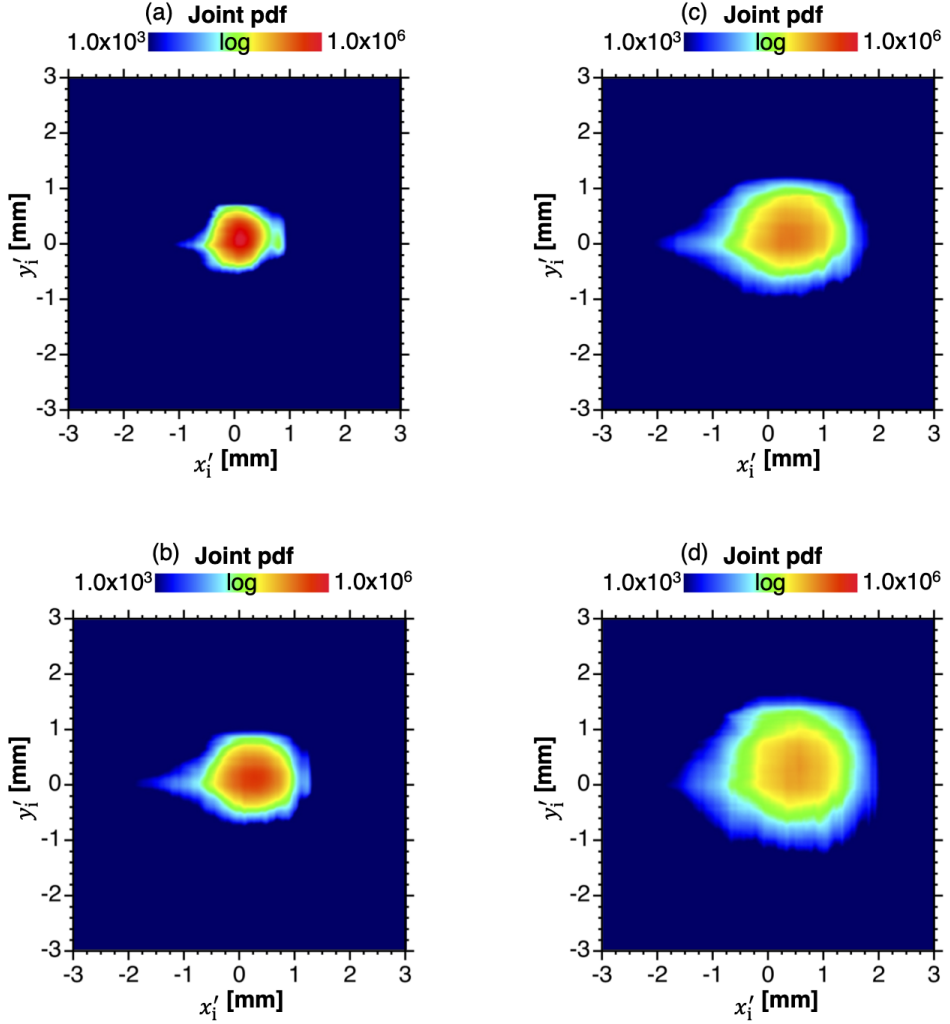


Figure 37: Joint pdf for $2\text{H}_2-\text{O}_2$ between the fluctuations of longitudinal displacements x'_i and that of the transverse displacements y'_i for different times from shock passage: (a) 2 μs , (b) 4 μs , (c) 6 μs , (d) 8 μs .

$$1006 \quad \sigma_{x'_i(t_0)x'_i(t_0+\tau_c)} = \frac{\frac{1}{N_c} \sum_{i=1}^{N_c} (x'_i(t_0) - \overline{x'_i(t_0)})(x'_i(t_0 + \tau_c) - \overline{x'_i(t_0 + \tau_c)})}{\sqrt{\frac{1}{N_c} \sum_{i=1}^{N_c} (x'_i(t_0) - \overline{x'_i(t_0)})^2} \sqrt{\frac{1}{N_c} \sum_{i=1}^{N_c} (x'_i(t_0 + \tau_c) - \overline{x'_i(t_0 + \tau_c)})^2}} \quad (\text{C } 3)$$

$$1007 \quad \sigma_{y'_i(t_0)y'_i(t_0+\tau_c)} = \frac{\frac{1}{N_c} \sum_{i=1}^{N_c} y'_i(t_0)y'_i(t_0 + \tau_c)}{\sqrt{\frac{1}{N_c} \sum_{i=1}^{N_c} y'_i(t_0)y'_i(t_0)} \sqrt{\frac{1}{N_c} \sum_{i=1}^{N_c} y'_i(t_0 + \tau_c)y'_i(t_0 + \tau_c)}} \quad (\text{C } 4)$$

1009 Here, N_c is the number of Lagrangian particles inside the computational domain at $t_0 + \tau_c$.

Mixture	Value				
2H ₂ -O ₂ -7Ar	Time from shock passage [μ s]	5.0	10.0	15.0	20.0
	Roundness [mm]	0.51	0.55	0.97	0.89
	Relative roundness [%]	36.0	28.0	35.0	30.0
	Offset in x direction [mm]	0.14	0.31	0.49	0.61
	Offset in y direction [mm]	0.07	0.13	0.28	0.30
2H ₂ -O ₂	Time from shock passage [μ s]	2.0	4.0	6.0	8.0
	Roundness [mm]	0.55	0.86	0.77	1.38
	Relative roundness [%]	39.0	45.0	34.0	46.0
	Offset in x direction [mm]	0.11	0.11	0.23	0.38
	Offset in y direction [mm]	0.12	0.14	0.22	0.29

Table 6: Roundness and offset from the center in Joint pdf for the fluctuations of longitudinal displacements and that of the transverse displacements.

Mixture	Characteristic times	Averaging procedure		
		Eulerian	Lagrangian (distance)	Lagrangian (time)
2H ₂ -O ₂ -7Ar	Induction time	0.9	1.0	0.9
	Reaction time	1.7	1.7	1.7
	Hydrodynamic thickness time	55.5	56.3	56.4
	Characteristic time for cell (cell length/ D_{CJ})	6.6	-	-
2H ₂ -O ₂	Induction time	0.6	0.7	0.6
	Reaction time	0.3	0.3	0.3
	Hydrodynamic thickness time	48.4	54.7	50.0
	Characteristic time for cell (cell length/ D_{CJ})	4.3	-	-

Table 7: Characteristic times normalized by induction time for 2H₂-O₂-7Ar and 2H₂-O₂ mixtures. The Lagrangian (distance) stands for the averaging process, described by Eqs. 4.12,4.14 and Lagrangian (time) refers to procedure based on Eqs. 4.11,4.13.

- 1010 ABDERRAHMANE, H. A., PAQUET, F., NG, H. D. 2011 Applying nonlinear dynamics theory to one-dimensional
1011 pulsating detonations, *Combust. Theory Model.*, **15**, pp. 205-225.
- 1012 ANAND, V., GUTMARK, E. 2019 Rotating detonation combustors and their similarities to rocket instabilities,
1013 *Prog. Energy Combust. Sci.*, **73**, pp. 182-234.
- 1014 AUSTIN, J. M. 2003 The role of instability in gaseous detonation PhD thesis California Institute of Technology.
- 1015 AUSTIN, J. M., PINTGEN, F., SHEPHERD, J. E. 2005 Reaction zone in highly unstable detonations, *Proc.*
1016 *Combust. Inst.*, **30**, pp. 1849-1857.
- 1017 BABIANO, A., BASDEVANT, C., ROY, P. L., SADOURNY, R. 1990 Relative dispersion in two-dimensional
1018 turbulence, *J. Fluid Mech.*, **214**, pp. 535-557.
- 1019 BOFFETTA, G., CELANI, A., CRISANTI, A., VULPIANI, A. 1999 Pair dispersion in synthetic fully developed
1020 turbulence, *Phys. Rev. E*, **60**, pp. 6734-6741.
- 1021 BOFFETTA, G., SOKOLOV, I. M. 2002 Statistics of two-particle dispersion in two-dimensional turbulence,
1022 *Phys. Fluids*, **14**, pp. 3224-3232.
- 1023 BORZOU, B. 2016 Lagrangian trackers to investigate the detonation dynamics [http://detonationlab.
1024 blogspot.ca/2016/05/lagrangian-trackers-to-investigate.html](http://detonationlab.blogspot.ca/2016/05/lagrangian-trackers-to-investigate.html).
- 1025 BOURGOIN, M., OUELLETTE, N. T., XU, H., BERG, J., BODENSCHATZ, E. 2006 The role of pair dispersion in
1026 turbulent flow, *Science*, **311**, pp. 835-838.

- 1027 BUARIA, D., SAWFORD, B. L., YEUNG, P. K. 2015 Characteristics of backward and forward two-particle
1028 relative dispersion in turbulence at different Reynolds numbers, *Phys. Fluids*, **27**, 105101.
- 1029 BUCKMASTER, J. 1989 A theory for triple point spacing in overdriven detonation waves, *Combust. Flame*,
1030 **77**, pp. 219-228.
- 1031 BUCKMASTER, J. D., LUDFORD, G. S. S. 1986 The effect of structure on the stability of detonations I. Role of
1032 the induction zone, *Proc. Combust. Inst.*, **21**, pp. 1669-1676.
- 1033 CHAPMAN, S., COWLING, T. G. 1991 *The Mathematical Theory of Non-uniform Gases*, 3rd edition, Cambridge
1034 University Press.
- 1035 CHINNAYYA, A., HADJADI, A., NGOMO, D. 2013 Computational study of detonation wave propagation in
1036 narrow channels, *Phys. Fluids*, **25**, 036101.
- 1037 CHIQUETE, C., SHORT, M. 2019 Characteristic path analysis of confinement influence on steady two-
1038 dimensional detonation propagation, *J. Fluid Mech.*, **863**, pp. 789-816.
- 1039 CRANE, J., LIPKOWICZ, J. T., SHI, X., WLOKAS, I., KEMPF, A. M., WANG, H. 2023 Three-dimensional
1040 detonation structure and its response to confinement, *Proc. Combust. Inst.*, **39**, pp. 2915-2923.
- 1041 CRANE, J., SHI, X., LIPKOWICZ, J. T., KEMPF, A. M., WANG, H. 2021 Geometric modeling and analysis of
1042 detonation cellular stability, *Proc. Combust. Inst.*, **38**, pp. 3585-3593.
- 1043 DARRAGH, R., TOWERY, Z., POLUDNENKO, A. Y., HAMLINGTON, P. E. 2021 Particle pair dispersion and eddy
1044 diffusivity in a high-speed premixed flame, *Proc. Combust. Inst.*, **38**, pp. 2845-2852.
- 1045 DESBORDES, D., PRESLES, H. N. 2012 Multi-scaled cellular detonation *Shock Waves Science and Technology*
1046 *Library*, vol. 6., (ed. Zhang, F.), pp. 281-338.
- 1047 ECKETT, C. A., QUIRK, J. J., SHEPHERD, J. E. 2000 The role of unsteadiness in direct initiation of gaseous
1048 detonations, *J. Fluid Mech.*, **421**, pp. 147-183.
- 1049 EDWARDS, D. H., JONES, A. T., PHILLIPS, D. E. 1976 The location of the Chapman-Jouguet surface in a
1050 multiheaded detonation wave, *J. Phys. D. Appl. Phys.*, **9**, pp. 1331-1342.
- 1051 EMMONS, H. W. 1958 Flow discontinuities associated with combustion. *Fundamentals of Gas Dynamics*
1052 *in High Speed Aerodynamics and Jet Propulsion* (ed. H. W. Emons) Princeton University Press
1053 Princeton.
- 1054 FARIA, L. M. 2014 Qualitative and asymptotic theory of detonations PhD thesis King Abdullah University
1055 of Science and Technology.
- 1056 FAVRE A. 1965 Equation des gas turbulents compressibles, *J. Méc.*, **4**, pp. 361-421.
- 1057 FICKE, W., W. C. DAVIS 2000 *Detonation Theory and Experiment*, Dover Publication.
- 1058 GAMEZO, V. N., DESBORDES, D., ORAN, E. S. 1999a Formation and evolution of two-dimensional cellular
1059 structure, *Combust. Flame*, **116**, pp. 154-165.
- 1060 GAMEZO, V. N., DESBORDES, D., ORAN, E. S. 1999b Two-dimensional reactive flow dynamics in cellular
1061 detonation waves, *Shock Waves*, **9**, pp. 11-17.
- 1062 GAMEZO, V. N., VASIL'EV, A. A., KHOKHLOV, A. M., ORAN, E. S. 2000 Fine cellular structure produced by
1063 marginal detonations, *Proc. Combust. Inst.*, **28**, pp. 611-617.
- 1064 GORDON, S., MCBRIDE, B. J., ZELEZNIK, F. J. 1984 Computer program for calculation of complex chemical
1065 equilibrium compositions and applications supplement I - transport properties, *Tech. Rep.* 86885
1066 NASA Tech. Mem.
- 1067 GOTTLIEB, S., SHU, C., TADMOR, E. 2001 Strong stability-preserving high-order time discretization methods,
1068 *SIAM rev.*, **43**, pp. 89-112.
- 1069 GOU, X., SUN, W., CHEN, Z., JU, Y. 2010 A dynamic multi-timescale method for combustion modeling with
1070 detailed and reduced chemical kinetic mechanism, *Combust. Flame*, **157**, pp. 1111-1121.
- 1071 HAN, W., KONG, W., GAO, Y., LAW, C. K. 2017 The role of global curvature on the structure and propagation
1072 of weakly unstable cylindrical detonations, *J. Fluid Mech.*, **813**, pp. 458-481.
- 1073 HAN, W., WANG, C., LAW, C. K. 2019 Role of transversal concentration gradient in detonation propagation,
1074 *J. Fluid Mech.*, **865**, pp. 602-649.
- 1075 HENRICK, A. K., ASLAM, T. D., POWERS, J. M. 2006 Simulations of pulsating one-dimensional detonations
1076 with true fifth order accuracy, *J. Comput. Phys.*, **213**, pp. 311-329.
- 1077 HIGGINS, A. 2012 Steady one-dimensional detonations, In *Shock Waves Science and Technology Library*
1078 (Chap. 2), **Vol. 6**, pp. 33-105. Ed. F. Zhang. Springer, Berlin, Heidelberg.
- 1079 HONG, Z., DAVIDSON, D. F., HANSON, R. K. 2011 An improved H₂/O₂ mechanism based on recent shock
1080 tube/laser absorption measurements, *Combust. Flame*, **158**, pp. 633-644.
- 1081 HU, F., WANG, R., CHEN, X. 2016 A modified fifth-order WENOZ method for hyperbolic conservation laws,
1082 *J. Comput. Appl. Math.*, **303**, pp. 56-68.

- 1083 JARSALÉ, G., VIROT, F., CHINNAYYA, A. 2016 Ethylene-air detonation in water spray, *Shock Waves*, **26**, pp.
1084 561-572.
- 1085 JOURDAINE, J., TSUBOI, N., HAYASHI, A. K. 2022 Investigation of liquid n-heptane/air spray detonation with
1086 an Eulerian-Eulerian model, *Combust. Flame*, **244**, 112278.
- 1087 JULLIEN, M., PARET, J., TABELING, P. 1999 Richardson pair dispersion in two-dimensional turbulence, *Phys.*
1088 *Rev. Lett.*, **82**, pp. 2872-2875.
- 1089 KANESHIGE, M., SHEPHERD, J. E. 1997 Detonation database, *GALCIT Report FM97-8*, California Institute
1090 of Technology
- 1091 KASIMOV, A. R., STEWART, D. S. 2004 On the dynamics of self-sustained one-dimensional detonations: a
1092 numerical study in the shock-attached frame, *Phys. Fluids*, **16**, pp. 3566-3578.
- 1093 KEE, R. J., COLTRIN, M. E., GLARBORG, P. 2003 Chemically reacting flow Theory and Practice, John Wiley
1094 & Sons, Inc.
- 1095 KIM, K. H., KIM, C., RHO, O. 2001 Methods for the accurate computations of hypersonic flows: I. AUSMPW+
1096 scheme, *J. Comput. Phys.*, **174**, pp. 33-80.
- 1097 KIYANDA, C. B., HIGGINS, A. J. 2013 Photographic investigation into the mechanism of combustion in
1098 irregular detonation waves, *Shock Waves*, **23**, pp. 115-130.
- 1099 LALCHANDANI, S. 2022 Modelling of quasi steady detonations with inert confinement Master thesis
1100 University of Ottawa.
- 1101 LAU-CHAPDELAINÉ, S. S.-M., XIAO, Q., RADULESCU, M. I. 2021 Viscous jetting and Mach stem bifurcation
1102 in shock reflections: experiments and simulations, *J. Fluid Mech.*, **908**, A18.
- 1103 LAW, C. K. 2006 Combustion Physics, Cambridge University Press.
- 1104 LEE, J. H. S. 2008 The Detonation Phenomenon, Cambridge University Press.
- 1105 LEE, J. H. S., RADULESCU, M. I. 2005 On the hydrodynamic thickness of cellular detonations, *Combust.*
1106 *Explos. Shock Waves*, **15**, pp. 205-225.
- 1107 MAXWELL, B. M., BHATTACHARJEE, R. R., LAU-CHAPDELAINÉ, S. S. M., FALLE, S. A. E. G., SHARPE, G. J.,
1108 RADULESCU, M. I. 2017 Influence of turbulent fluctuation on detonation propagation, *J. Fluid Mech.*,
1109 **818**, pp. 646-696.
- 1110 MAXWELL, B. M., PEKALSKI, A., RADULESCU, M. I. 2018 Modelling of the transition of a turbulent shock-
1111 flame complex to detonation using the linear eddy model, *Combust. Flame*, **192**, pp. 340-357.
- 1112 MAZAHERI, K., MAHMOUDI, Y., RADULESCU, M. I. 2012 Diffusion and hydrodynamic instabilities in gaseous
1113 detonations, *Combust. Flame*, **159**, pp. 2138-2154.
- 1114 MCBRIDE, B. J., GORDON, S., RENO, M. A. 1993 Coefficients for calculating thermodynamic and transport
1115 properties of individual species, *Tech. Rep.* 4513 NASA Tech. Mem.
- 1116 MÉVEL, R., GALLIER, S. 2018 Structure of detonation propagating in lean and rich dimethyl ether-oxygen
1117 mixtures, *Shock Waves*, **28**, pp. 955-966.
- 1118 MI, X., TANG YUK, K. C., LEE, J. H. S., NG, H. D., HIGGINS, A. J., NIKIFORAKIS, N. 2018 An approach
1119 to measure the hydrodynamic thickness of detonations in numerical simulations, 37th International
1120 Symposium on Combustion, Poster
- 1121 MI, X., TIMOFEEV, E. V., HIGGINS, A. J. 2017a Effect of spatial discretization of energy on detonation wave
1122 propagation, *J. Fluid Mech.*, **817**, pp. 306-338.
- 1123 MI, X., HIGGINS, A. J., NG, H. D., KIYANDA, C. B., NIKIFORAKIS, N. 2017b Propagation of gaseous detonation
1124 waves in a spatially inhomogeneous reactive medium, *Phys. Rev. Fluids*, **2**, 053201.
- 1125 MÖLDER, S. 2016 Curved shock theory, *Shock Waves*, **26**, pp. 337-353.
- 1126 MONNIER, V., RODRIGUEZ, V., VIDAL, P., ZITOUN, R. 2022 An analysis of three-dimensional patterns of
1127 experimental detonation cells, *Combust. Flame*, **245**, 112310.
- 1128 MURRAY, S. B., LEE, J. H. 1983 On the transformation of Planar Detonation to Cylindrical Detonation,
1129 *Combust. Flame*, **52**, pp. 262-289.
- 1130 MURRAY, S. B., LEE, J. H. 1985 The influence of yielding confinement on large-scale ethylene-air detonations,
1131 *Dynamics of Shock Waves, Explosion, and Detonations*, pp. 80-103.
- 1132 MURRAY, S. B., LEE, J. H. 1986 The influence of physical boundaries on gaseous detonation waves, *Prog.*
1133 *Astronaut. Aero.*, **106**, pp. 329-355.
- 1134 NEUFELD, P. D., JANZEN A. R., AZIZ R. A. 1972 Empirical equations to calculate 16 of the transport collision
1135 integral $\Omega^{(l,s)*}$ for the Lennard-Jones (12-6) potential, *J. Chem. Phys.*, **57**, pp. 1100-1102.
- 1136 NG, H. D., HIGGINS, A. J., KIYANDA, C. B., RADULESCU, M. I., LEE, J. H. S., BATES, K. R., NIKIFORAKIS, N.
1137 2005a Nonlinear dynamics and chaos analysis of one-dimensional pulsating detonations, *Combust.*
1138 *Theory Model.*, **9**, pp. 159-170.

- 1139 NG, H. D., RADULESCU, M. I., HIGGINS, A. J., NIKIFORAKIS, N., LEE, J. H. S. 2005b Numerical investigation
1140 of the instability for one-dimensional Chapman-Jouguet detonations with chain-branching kinetics,
1141 *Combust. Theory Model.*, **9**, pp. 385-401.
- 1142 ORAN, E. S., CHAMBERLAIN, G., PEKALSKI, A. 2020 Mechanism and occurrence of detonation in vapor
1143 cloud explosions, *Prog. Energy Combust. Sci.*, **77**, 100804.
- 1144 PINTGEN, F., ECKETT, C. A., AUSTIN, J. M., SHEPHERD, J. E. 2003 Direct observations of reaction zone in
1145 propagating detonations, *Combust. Flame*, **133**, pp. 211-229.
- 1146 POLING, B. E., PRAUSNITZ, J. M., O'CONNEL, J. P. 2001 *The Properties of Gases and Liquids*, 5th edition,
1147 McGraw-Hill Education
- 1148 RADULESCU, M. I. 2003 *The propagation and failure mechanism of gaseous detonations: experiments in
1149 porous-walled tubes* PhD thesis McGill University.
- 1150 RADULESCU, M. I. 2018 A detonation paradox: Why inviscid detonation simulations predict the incorrect
1151 trend for the role of instability in gaseous cellular detonations?, *Combust. Flame*, **195**, pp. 151-162.
- 1152 RADULESCU, M. I., LEE, J. H. S. 2002 The failure mechanism of gaseous detonations: experiment in porous
1153 wall tube, *Combust. Flame*, **131**, pp. 29-46.
- 1154 RADULESCU, M. I., SHARPE, G. J., BRADLEY, D. 2013 A universal parameter quantifying explosion hazards,
1155 detonability and hot spot formation: the χ number, *Proc. of the Seventh International Seminar on
1156 Fire & Explosion Hazards (ISFEH7)*, pp. 1-13.
- 1157 RADULESCU, M. I., SHARPE, G. J., LAW, C. K., LEE, J. H. S. 2007 The hydrodynamic structure of unstable
1158 cellular detonations, *J. Fluid Mech.*, **580**, pp. 31-81.
- 1159 RADULESCU, M. I., SHARPE, LEE, J. H. S., KIYANDA, C. B., HIGGINS, A. J., HANSON, R. K. 2005 The ignition
1160 mechanism in irregular structure gaseous detonations, *Proc. Combust. Inst.*, **30**, pp. 1859-1867.
- 1161 REACTION DESIGN. 2000 Transport a software package for the evaluation of gas-phase, multicomponent
1162 transport properties, TRA-036-1.
- 1163 REYNAUD, M., TAILEB, S., CHINNAYYA, A. 2020 Computation of the mean hydrodynamic structure of
1164 gaseous detonation with losses, *Shock Waves*, **30**, pp. 645-669.
- 1165 REYNAUD, M., VIROT, F., CHINNAYYA, A. 2017 A computational study of the interaction of gaseous detonation
1166 with a compressible layer, *Phys. Fluids*, **29**, 056101.
- 1167 RICHARDSON, L. F. 1926 Atmospheric diffusion shown on a distance-neighbour graph, *Proc. R. Soc. Lond.
1168 Ser. A.*, **110**, pp. 709-737.
- 1169 ROMICK, C. M., ASLAM, T. D., POWER, J. M. 2012 The effect of diffusion on the dynamics of unsteady
1170 detonations, *J. Fluid Mech.*, **699**, pp. 453-464.
- 1171 SALAZAR, J. P. L. C., COLLINS, L. R. 2009 Two-particle dispersion in isotropic turbulent flows, *Annu. Rev.
1172 Fluid Mech.*, **41**, pp. 405-432.
- 1173 SAWFORD, B. 2001 Turbulent relative dispersion, *Annu. Rev. Fluid Mech.*, **33**, pp. 289-317.
- 1174 SAWFORD, B. L., POPE, S. B., YEUNG, P. K. 2013 Gaussian Lagrangian stochastic models for multi-particle
1175 dispersion, *Phys. Fluids*, **25**, 055101.
- 1176 SCATAMACCHIA, R., BIFERALE, L., TOSCHI, F. 2012 Extreme events in the dispersions of two neighboring
1177 particles under the influence of fluid turbulence, *Phys. Rev. Lett.*, **109**, 144501.
- 1178 SHARPE, G. J. 2002 Shock-induced ignition for a two-step chain-branching kinetics model, *Phys. Fluids*, **14**,
1179 pp. 4372-4388.
- 1180 SHEPHERD, J. E. 2009 Detonation in gases, *Proc. Combust. Inst.*, **32**, pp. 83-98.
- 1181 SHI, L., SHEN, H., ZHANG, P., ZHANG, D., WEN, C. 2017 Assessment of vibrational non-equilibrium effect
1182 on detonation cell size, *Combust. Sci. Tech.*, **189**, pp. 841-853.
- 1183 SHIMURA, K., MATSUO, A. 2018 Two-dimensional CFD-DEM simulation of vertical shock wave-induced
1184 dust lifting process, *Shock Waves*, **28**, pp. 1285-1297.
- 1185 SHORT, M., QUIRK, J. J. 2018 High explosive detonation-confiner interactions, *Annu. Rev. Fluid Mech.*, **50**,
1186 pp. 215-242.
- 1187 SOKOLOV, I. M. 1999 Two-particle dispersion by correlated random velocity fields, *Phys. Rev. E*, **60**, pp.
1188 5528-5532.
- 1189 SOW, A., CHINNAYYA, A. HADJADI, A. 2014 Mean structure of one-dimensional unstable detonations with
1190 friction, *J. Fluid Mech.*, **743**, pp. 503-533.
- 1191 SOW, A., CHINNAYYA, A. HADJADI, A. 2015 Computational study of non-ideal and mildly-unstable detonation
1192 waves, *Compt. Fluids*, **119**, pp. 47-57.
- 1193 SOW, A., CHINNAYYA, A. HADJADI, A. 2019 On the viscous boundary layer of weakly unstable detonations
1194 in narrow channels, *Compt. Fluids*, **179**, pp. 449-458.

- 1195 SOW, A., LAU-CHAPDELAINE, S. M., RADULESCU, M. I. 2021 The effect of the polytropic index γ on the
1196 structure of gaseous detonations, *Proc. Combust. Inst.*, **38**, pp. 3633-3640.
- 1197 STEWART, D. S., KASIMOV, A. R. 2005 Theory of detonation with an embedded sonic locus, *SIAM J. Appl.*
1198 *Math.*, **66**, pp. 384-407.
- 1199 STREHLOW, R. A. 1970 Multi-dimensional detonation wave structure, *Astronaut. Acta*, **15**, pp. 345-357.
- 1200 TANG, J., RADULESCU, M. I. 2013 Dynamics of shock induced ignition in Fickett's model: Influence of χ ,
1201 *Proc. Combust. Inst.*, **34**, pp. 2035-2041.
- 1202 TAILEB, S. 2020 Vers des simulations numériques prédictives des détonations gazeuses - Influence de la
1203 cinétique chimique, de l'équation d'état et des effets tridimensionnels PhD thesis ISAE-ENSMA.
- 1204 TAILEB, S., REYNAUD, M., CHINNAYYA, A., VIROT, F., BAUER, P. 2018 Numerical study of 3D gaseous
1205 detonations in a square channel, *Aerotec. Missili Spaz.*, **97**, pp. 96-102.
- 1206 TAILEB, S., MELUGUIZO-GAVILANCES, J., CHINNAYYA, A. 2021 Influence of the chemical modeling on the
1207 quenching limits of gaseous detonation waves confined by an inert layer, *Combust. Flame*, **218**, pp.
1208 247-259.
- 1209 TAILEB, S., MELUGUIZO-GAVILANCES, J., CHINNAYYA, A. 2021 The influence of the equation of state on the
1210 cellular structure of gaseous detonations, *Phys. Fluids*, **33**, 036105.
- 1211 TAYLOR, B. D., KESSLER, D. A., GAMEZO, V. N., ORAN, E. S. 2013 Numerical simulations of hydrogen
1212 detonations with detailed chemical kinetics, *Proc. Combust. Inst.*, **34**, pp. 2009-2016.
- 1213 VASILEV, A. A., NIKOLAEV, Y. 1978 Closed theoretical model of a detonation cell, *Acta Astronaut.*, **5**, pp.
1214 983-996.
- 1215 VASIL'EV, A. A., GAVRILENKO, T. P., MITROFANOV, V. V., SUBBOTIN, V. A., TOPCHIYAN, M. E. 1972 Location
1216 of the sonic transition behind a detonation front, *Combust. Explos. Shock Waves*, **8**, pp. 80-84.
- 1217 WARNATZ J., MAAS U., DIBBLE R. W. 2006 Combustion: Physical and Chemical Fundamentals, Modeling
1218 and Simulation, Experiments, Pollutant Formation, 4th Edition, Springer.
- 1219 WATANABE, H. 2020 Gaseous detonation with dilute water spray in a two-dimensional straight channel:
1220 analysis based on numerical simulation, PhD thesis, Keio University
- 1221 WATANABE, H., MATSUO, A., CHINNAYYA, A., MATSUOKA, K., KAWASAKI, A., KASAHARA, J. 2020 Numerical
1222 analysis of the mean structure of gaseous detonation with dilute water spray, *J. Fluid Mech.*, **887**,
1223 A4.
- 1224 WATANABE, H., MATSUO, A., CHINNAYYA, A., MATSUOKA, K., KAWASAKI, A., KASAHARA, J. 2021 Numerical
1225 analysis on behavior of dilute water droplets in detonation, *Proc. Combust. Inst.*, **38**, pp. 3709-3716.
- 1226 WATANABE, H., MATSUO, A., MATSUOKA, K., KAWASAKI, A., KASAHARA, J. 2019 Numerical investigation on
1227 propagation behavior of gaseous detonation in water spray, *Proc. Combust. Inst.*, **37**, pp. 3617-3626.
- 1228 WEBER, M., OLIVIER, H. 2003 The thickness of detonation waves visualised by slight obstacles, *Shock*
1229 *Waves*, **13**, pp. 351-365.
- 1230 WILKE, C. R. 1958 A viscosity equation for gas mixtures, *J. Chem. Phys.*, **18**, pp. 517-519.
- 1231 WOLANSKI, P. 2013 Detonative propulsion, *Proc. Combust. Inst.*, **34**, pp. 125-158.
- 1232 XIA, H., FRANCOIS, N., FABER, B., PUNZMANN, H., SHATS, M. 2019 Local anisotropy of laboratory two-
1233 dimensional turbulence affects pair dispersion, *Phys. Fluids*, **31**, 025111.
- 1234 XIAO, Q., RADULESCU, M. I. 2020 Dynamics of hydrogen-oxygen-argon cellular detonations with a constant
1235 mean lateral strain rate, *Combust. Flame*, **215**, pp. 437-457.
- 1236 ZHANG, F. 2012 Detonation Dynamics, Shock Wave Science and Technology Reference Library, Springer.
- 1237 ZHOU, Y., ZHANG, X., ZHONG, L., DEITERDING, R., ZHOU, L., WEI, H. 2022 Effects of fluctuation in
1238 concentration on detonation propagation, *Phys. Fluids*, **34**, 076101.